

Bending–compression coupling in extensible slender microswimmers

Kenta Ishimoto¹ , Johann Herault²  and Clément Moreau² 

¹Department of Mathematics, Kyoto University, Kyoto 606-8502, Japan

²Nantes Université, École Centrale Nantes, IMT Atlantique, CNRS, LS2N, UMR 6004, Nantes F-44000, France

Corresponding author: Kenta Ishimoto, kenta.ishimoto@math.kyoto-u.ac.jp

(Received 13 April 2025; revised 20 August 2025; accepted 23 August 2025)

Undulatory slender objects have been a central theme in the hydrodynamics of swimming at low Reynolds number, where the slender body is usually assumed to be inextensible, although some microorganisms and artificial microrobots largely deform with compression and extension. Here, we theoretically study the coupling between the bending and compression/extension shape modes, using a geometrical formulation of kinematic microswimmer hydrodynamics to deal with the non-commutative effects between translation and rotation. By means of a coarse-grained minimal model and systematic perturbation expansions for small bending and compression/extension, we analytically derive the swimming velocities and report three main findings. First, we revisit the role of anisotropy in the drag ratio of the resistive force theory, and generally demonstrate that no motion is possible for uniform compression with isotropic drag. We then find that the bending–compression/extension coupling generates lateral and rotational motion, which enhances the swimmer’s manoeuvrability, as well as changes in progressive velocity at a higher order of expansion, while the coupling effects depend on the phase difference between the two modes. Finally, we demonstrate the importance of often-overlooked Lie bracket contributions in computing net locomotion from a deformation gait. Our study sheds light on compression as a forgotten degree of freedom in swimmer locomotion, with important implications for microswimmer hydrodynamics, including understanding of biological locomotion mechanisms and design of microrobots.

Key words: biological fluid dynamics, micro-organism dynamics, propulsion

1. Introduction

The hydrodynamics of swimming of slender bodies in the Stokes regime has been intensively studied in recent decades, in particular in the context of swimming

microorganisms with cilia and flagella, and artificial microrobots made of rod-shaped particles and flexible filaments (Elgeti, Winkler & Gompper 2015; Lauga 2020). The locomotion of such swimmers is often achieved by undulatory deformation, therefore studies on a bending filament in a viscous fluid have constituted a central theme in the field for more than a half century (Taylor 1951; Gray & Hancock 1955). These slender objects are usually assumed to be inextensible, although this assumption may not be reasonable for some biological and artificial swimmers.

In fact, large compressions and extensions have been reported in some unicellular microorganisms. A slender organelle, spasmoneme, seen in *Vorticella*, can rapidly contract within a second in response to calcium signalling (Ryu *et al.* 2016), with its contraction being rather uniform. A microtubule-based motile organelle, called haptonema, seen in Haptophyte algae, exhibits a rapid coiling contraction within milliseconds, while the detailed mechanisms are still unknown (Nomura *et al.* 2019). Microtubule-supported pseudopodia of Heliozoan, called axopodia, also exhibit contraction and extension (Suzaki *et al.* 1980; Febvre-Chevalier & Febvre 1986). Body contraction is well known in *Euglena* as euglenoid motion (Arroyo *et al.* 2012), and such a body contraction is also seen in some ciliates such as *Stentor* (Huang & Pitelka 1973). More recently, an origami-based mechanism has been uncovered for a large extensibility of a ‘neck’ of *Lacrymaria* (Flaum & Prakash 2024).

The millimetre-sized nematode *Caenorhabditis elegans* is a well-studied model organism in a large domain of biology, including reproduction, development and neuromechanics (Meneely, Dahlberg & Rose 2019), and its swimming dynamics is also well captured by fluid mechanics in the Stokesian regime (Montenegro-Johnson *et al.* 2016). Since the bending motion of *C. elegans* is driven by muscular contraction, the worm inevitably changes its body length during its movement. Hence the measurement of compressibility has been performed experimentally, for example, by a linear viscoelastic model (Backholm, Ryu & Dalnoki-Veress 2013). The shape tracking through videomicroscopy also requires the body contraction/extension for accurate detection of the body shape (Roussel *et al.* 2014). Integrated neuromechanical models of *C. elegans* therefore include body extensibility (Izquierdo & Beer 2018).

In artificial microrobots, large compressions and extensions are well recognised in microswimmers made of hydrogels (Nikolov, Yeh & Alexeev 2015; Sharan *et al.* 2021; Tan *et al.* 2024). Motile extensible filament has been experimentally developed via a self-assembled droplet, in which self-elongation is essential to trigger morphological instability (Cholakova *et al.* 2021; Lisicki 2024).

The simplest model of the body–environment coupling of slender bodies in the inertialess regime is the resistive force theory (RFT), which only considers the local hydrodynamic drag and does not account for non-local hydrodynamic interactions (Gray & Hancock 1955; Lighthill 1976). Nonetheless, because of its theoretical and computational simplicity, RFT has been widely used as an empirical drag model of viscous Newtonian fluid as well as non-Newtonian fluid (Fu, Powers & Wolgemuth 2007; Riley & Lauga 2017) and granular material (Zhang & Goldman 2014). More recently, RFT-type local drag models have been used even for terrestrial locomotion, including slithering and legged animals and robots (Zhang & Goldman 2014; Chong *et al.* 2023; Rieser *et al.* 2024). In these studies with RFT, net locomotion is generated by the drag anisotropy between the tangential and normal drag coefficients.

Despite these broad interests in the compressible/extensible slender microswimming from biological to artificial systems, our understanding about the impact of compression/extension when coupled to bending deformation is still very limited, even in the kinematic swimming problem where the swimmer shape gait is prescribed. Notable past theoretical

studies on the role of compression/extension in kinematic microswimming deal with an extensible filament with isotropic drag ratio that moves in one dimension (Pak & Lauga 2011), and a slender helical body, numerically simulated with implicit extensibility by reparametrisation of the body curve (Pak *et al.* 2012). Another model featuring compression was studied in the context of crawling worm motions (DeSimone & Tatone 2012; Tanaka *et al.* 2012), which, however, focused on body–surface interactions with one-dimensional locomotion, and does not contain a bending mode. Body extensibility was considered in simulations of an active filament in a viscous fluid, but mainly to stabilise the numerical schemes (Olson, Lim & Cortez 2013; Ishimoto & Gaffney 2018).

An exception is the kinematic two-link scallop swimmer with compression/extension, which has been studied recently by Gidoni, Morandotti & Zoppello (2024), focusing on the controllability problem. The famous Purcell scallop theorem (Purcell 1977; Ishimoto & Yamada 2012) states that a reciprocal deformation cycle cannot generate net locomotion in Stokes flow. Since compression/extension provides an additional degree of freedom, even the simple scallop model with a single bending angle can generate net locomotion. To the best of the authors' knowledge, however, the impacts of the compression/extension during bending motions have not been studied comprehensively.

Our aim in this study is therefore to theoretically elucidate the mechanical coupling between body compression/extension and bending of self-propelled kinematic slender bodies at low Reynolds number, which we hereafter refer to as the *bending–compression* coupling for brevity. For this purpose, we use the geometrical theory of microswimming (Shapere & Wilczek 1989), which relies on the connection operator linking net motion as the product of a cyclic body deformation. The swimmer trajectories are obtained by a geometrical integration based on the Magnus expansion (Hatton & Choset 2015), with Lie brackets capturing the effects of motion non-commutativity.

Equipped with this framework, we make further analytical progress by two methods: coarse-graining the deformation of the swimmer to a minimal set of two degrees of freedom, and focusing on small-amplitude deformation in the general case. Regarding the choice of deformation cycles, we examine two illustrative examples, uniform compression and bending–compression wave, motivated by biological locomotion such as body contraction of unicellular microorganisms and muscular contraction of nematodes.

Upon laying out the dynamics and deriving analytical expressions for the coarse-grained and small-amplitude cases, our results on the bending–compression dynamics in slender microswimmers may be outlined as three main findings. First, we demonstrate that bending–compression coupling allows net locomotion in the case of isotropic drag, even if the swimmer's total body length remains constant over time, rectifying a prior statement by Pak & Lauga (2011) that overlooked the active role of local compression. Second, we observe the prominent role played by bending–compression coupling in enhancing the swimmer's ability to rotate in the fixed frame, through the emergence of a coupled lower-order term in the averaged rotational velocity from small-amplitude theory. This improved turning ability is also confirmed by numerical simulations at large amplitude. Finally, the expressions that we obtain for swimming velocity through perturbative analysis highlight the importance of the Lie bracket terms due to non-commutativity between rotation and translation in deriving the swimmer's net locomotion, which is often bypassed in analogous studies on flagellar swimming. The bending–compression swimmer provides an instructive example warranting the crucial role of non-commutative terms in a broader context of microswimming theory.

The paper is organised as follows. In § 2, we introduce our general compressible/extensible slender object, and present a general statement on locomotion with isotropic drag. In § 3, we consider a minimal theoretical model similar to the compressible/

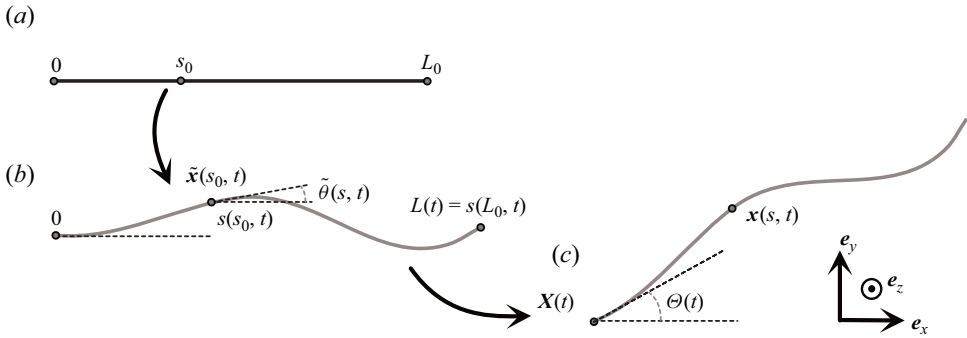


Figure 1. Schematic of a filament in three frames of reference. (a) A filament in a reference state. The arc length $s_0 \in [0, L_0]$ is used for parametrisation of the curve. (b) A filament in the body-fixed frame at time t . The point labelled by s_0 is mapped to $\tilde{\mathbf{x}}(s_0, t)$, where the distance along the filament is denoted by $s(s_0, t)$, and the local tangent angle is represented as $\tilde{\theta}(s, t)$. (c) A filament in the laboratory frame, which is obtained by rigid body transformation, translation with $\mathbf{X}(t)$, and rotation by $\Theta(t)$, from the filament in (b). The point $\tilde{\mathbf{x}}(s_0, t)$ is mapped to $\mathbf{x}(s, t)$.

extensible scallop swimmer by Gidoni *et al.* (2024), focusing on elementary locomotion gaits and the case of isotropic drag. We then analyse a general slender object via a systematic perturbation theory on small-amplitude bending and compression in §4. Two example swimmers, uniform compression and bending–compression wave, are then examined in §§5 and 6, respectively, followed by a discussion on swimmer manoeuvrability by compression in §7, before final conclusions are drawn in §8.

2. Problem setting and general properties

2.1. Coordinates, kinematics and dynamics

We consider a slender self-propelled object moving in a plane, which we denote as our x – y plane, as illustrated in figure 1. The shape of the slender filamentous object is described by its centreline curve. The length of the filament, L , may change over time due to self-compression/extension. To represent this effect, we introduce a Lagrangian label $s_0 \in [0, L_0]$ as the arc length of the filament in the reference state, where L_0 is the reference length of the filament (figure 1a). We then consider the compression/extension at time t in the form

$$\frac{\partial s}{\partial s_0} = 1 + \eta p(s_0, t), \quad (2.1)$$

where $s = s(s_0, t)$ is the arc length of the current configuration at time t (figure 1b). Here, we introduce a constant η for later use. The body-fixed frame is introduced as a frame attached to the leftmost point of the slender body, as shown in figure 1(b). The position labelled by s_0 is deformed to $\tilde{\mathbf{x}}(s_0, t)$ in the body-fixed frame, and the tangent angle is given by $\tilde{\theta}(s_0, t)$. We describe self-deformation of the swimmer as

$$\tilde{\theta}(s_0, t) = \epsilon q(s_0, t), \quad (2.2)$$

where the constant ϵ is introduced for later use.

The body shape in the laboratory frame is obtained by a rigid body transformation, translation with $\mathbf{X}(t)$, and rotation by $\Theta(t)$, as in figure 1(c). The point $\tilde{\mathbf{x}}(s_0, t)$ in the body-fixed frame is then mapped to $\mathbf{x}(s, t)$ in the laboratory frame by $\mathbf{x} = \mathbf{X} + \mathbf{R}_\Theta \tilde{\mathbf{x}}$, where \mathbf{R}_Θ is the two-dimensional rotation matrix by an angle Θ . In this study, we consider the kinematic problem amounting to solving the displacement $\mathbf{X}(t)$ and $\Theta(t)$, where the

shape gait is provided by the two intrinsic functions, $p(s_0, t)$ and $q(s_0, t)$, that physically correspond to local extensibility and local bending angle, respectively.

The velocity of the local point on the body in the laboratory frame is obtained as the Lagrangian time derivative defined as $D\mathbf{x}/Dt = \partial\mathbf{x}(s_0, t)/\partial t$. To compute this, we introduce the linear velocity $\mathbf{U} = (U_x, U_y)^T$ and the angular velocity $\boldsymbol{\Omega} = \Omega\mathbf{e}_z$, with $\Omega = d\Theta/dt$; the superscript T denotes the transpose. The local velocity is then given by

$$\frac{D\mathbf{x}}{Dt} = \mathbf{U} + \boldsymbol{\Omega}\mathbf{e}_z \times \tilde{\mathbf{x}} + \mathbf{R}_\Theta \frac{D\tilde{\mathbf{x}}}{Dt}. \quad (2.3)$$

To determine the motion of the object, we calculate the drag forces acting on an infinitesimal segment of the filament via the empirical RFT. With $C_\parallel (>0)$ and $C_\perp (>0)$ being the tangential and normal hydrodynamic drag coefficients per unit length, the drag from the environment is obtained as

$$\mathbf{f}(s, t) = -C_\parallel \left(\frac{D\mathbf{x}}{Dt} \cdot \mathbf{e}_\parallel \right) \mathbf{e}_\parallel - C_\perp \left(\frac{D\mathbf{x}}{Dt} \cdot \mathbf{e}_\perp \right) \mathbf{e}_\perp, \quad (2.4)$$

where $\mathbf{e}_\parallel(s_0, t)$ and $\mathbf{e}_\perp(s_0, t)$ are tangential and normal unit vectors at the segment of the filament, respectively. The ratio $\gamma := C_\perp/C_\parallel$ is called the anisotropy ratio, and the particular case $\gamma = 1$ is called isotropic drag. In this study, we take this as an arbitrary positive value. For swimming in low Reynolds number flow, it is known that $\gamma \rightarrow 2$ in the slender filament limit (Gray & Hancock 1955), and empirically $\gamma = 1.5\text{--}1.8$ is used for flagella and cilia (Lighthill 1976; Friedrich *et al.* 2010). When the flagellum possesses an accessory hairy structure known as mastigonemes, however, the effective anisotropy ratio γ may be lower than unity (Brennen 1976; Asadzadeh *et al.* 2022). In contrast, locomotion of *C. elegans* on a gel-like structure is well described by a large anisotropy ratio $\gamma \approx 70$ (Keaveny & Brown 2017).

To close the system and calculate the locomotion velocity, we employ the force-free $\tilde{\mathbf{F}} = (\tilde{F}_x, \tilde{F}_y)^T = \mathbf{0}$ and torque-free $\tilde{\mathbf{M}} = M\mathbf{e}_z = \mathbf{0}$ conditions in the body-fixed frame:

$$\int_0^{L(t)} \tilde{\mathbf{f}}(s, t) ds = \int_0^{L(t)} \tilde{\mathbf{x}} \times \tilde{\mathbf{f}}(s, t) ds = \mathbf{0}, \quad (2.5)$$

where we employ the torque around the point $\mathbf{X}(t)$. Equations (2.4) and (2.5) yield a closed form for the kinematic problem, allowing us to uniquely determine \mathbf{X} and Θ from a given deformation p and q .

We denote the translational velocity in the body-fixed frame by $\tilde{\mathbf{U}} = (\tilde{U}_x, \tilde{U}_y)^T$, and introduce a 3×3 matrix representation of the Lie group $\mathcal{G} \in \text{SE}(2)$, also known as homogeneous representation, as

$$\mathcal{G} = \begin{pmatrix} \mathbf{R}_\Theta & \mathbf{X} \\ (0, 0) & 1 \end{pmatrix}, \quad (2.6)$$

and the associated Lie algebra $\mathfrak{se}(2)$, whose elements $\hat{\mathcal{A}}$ act on $\text{SE}(2)$ as $\dot{\mathcal{G}} = \mathcal{G}\hat{\mathcal{A}}$, with the matrix representation

$$\hat{\mathcal{A}} = \begin{pmatrix} 0 & \Omega & \tilde{U}_x \\ -\Omega & 0 & \tilde{U}_y \\ 0 & 0 & 0 \end{pmatrix}. \quad (2.7)$$

The ‘hat’ notation of $\hat{\mathcal{A}}$ is standard in solid mechanics and refers to the correspondence between the matrix representation of the Lie algebra $\mathfrak{se}(2)$ and its twist coordinates stacked in a vector (representation) $\mathcal{A} = (\hat{\mathcal{A}})^\vee = (\tilde{U}_x, \tilde{U}_y, \Omega)^T$.

To derive the expression in the laboratory frame, we directly solve the differential equation on the rigid body motion, and represent its solution as

$$\mathcal{G}(T) = \mathcal{G}(0) \bar{\mathcal{P}} \exp \left[\int_0^T \hat{\mathcal{A}}(t) dt \right], \quad (2.8)$$

where the symbol $\bar{\mathcal{P}}$ denotes the reverse path ordering operator (Shapere & Wilczek 1989). Using the Magnus expansion, this formal solution (2.8) may be expanded in a Lie brackets series as

$$\begin{aligned} \mathcal{G}(T) = \mathcal{G}(0) \exp & \left[\int_0^T \hat{\mathcal{A}}(t_1) dt_1 + \frac{1}{2} \int_0^T dt_1 \int_0^{t_1} dt_2 [\hat{\mathcal{A}}(t_1), \hat{\mathcal{A}}(t_2)] \right. \\ & \left. + \frac{1}{6} \int_0^T dt_1 \int_0^{t_1} dt_2 \int_0^{t_2} dt_3 ([\hat{\mathcal{A}}(t_1), [\hat{\mathcal{A}}(t_2), \hat{\mathcal{A}}(t_3)]] + [\hat{\mathcal{A}}(t_3), [\hat{\mathcal{A}}(t_2), \hat{\mathcal{A}}(t_1)]]) + \dots \right], \end{aligned} \quad (2.9)$$

where the bracket symbol represents the matrix commutator $[\hat{\mathcal{A}}(t_1), \hat{\mathcal{A}}(t_2)] = \hat{\mathcal{A}}(t_1) \hat{\mathcal{A}}(t_2) - \hat{\mathcal{A}}(t_2) \hat{\mathcal{A}}(t_1)$.

An alternative path to the computation of \mathcal{G} resorts to gauge field theory (Shapere & Wilczek 1989; Zhao *et al.* 2022). By linearity of the RFT, the matrix $\hat{\mathcal{A}}$ may be decomposed as

$$\hat{\mathcal{A}} = \sum_{\alpha} \hat{\mathcal{H}}_{\alpha} \dot{\sigma}_{\alpha}, \quad (2.10)$$

where σ_{α} ($\alpha = 1, 2, \dots, N$) is the shape variable, and N is the number of degrees of freedom in the shape space, with the overdot symbol denoting the time derivative. Here, $\hat{\mathcal{H}}_{\alpha}$ is called a gauge field or Stokes connection, as it depends only on the shape variables. A local connection maps a shape variation to a velocity for a given body shape, independent of swimmer position and orientation (Kelly & Murray 1995). Using the matrix representation of $\text{SE}(2)$, the connection $\hat{\mathcal{H}}_{\alpha}$ is represented by a third-rank tensor of dimensions $3 \times 3 \times N$; we may also ‘drop the hats’ in (2.10), using the twist coordinates \mathcal{A} , which would, in turn, represent the Stokes connection \mathcal{H}_{α} as a $3 \times N$ matrix $\mathcal{H} = (\mathbf{H}_x; \mathbf{H}_y; \mathbf{H}_{\theta})$, where the semicolon denotes vertical concatenation. The integral representation (2.8) is then rewritten as

$$\mathcal{G}(T) = \mathcal{G}(0) \bar{\mathcal{P}} \exp \left[\sum_{\alpha} \int_C \hat{\mathcal{H}}_{\alpha}(\boldsymbol{\sigma}) d\sigma_{\alpha} \right], \quad (2.11)$$

where C is a path in the shape space. We are particularly interested in the net locomotion caused by a periodic shape gait, which is represented by a closed loop in the shape space. In the small-amplitude case, by neglecting terms above third order in the expansions, the net locomotion is well described by a surface integral of the curvature in the shape space as (Hatton & Choset 2015)

$$\mathcal{G}(T) \approx \mathcal{G}(0) \exp \left[\sum_{\alpha, \beta} \int_{S_C} \hat{\mathcal{F}}_{\alpha\beta}(\boldsymbol{\sigma}) d\sigma_{\alpha} d\sigma_{\beta} \right], \quad (2.12)$$

where S_C is a region in the shape space enclosed by the close loop C , and the associated curvature form, also called field strength or Stokes curvature, is defined as

$$\hat{\mathcal{F}}_{\alpha\beta} = \frac{\partial \hat{\mathcal{H}}_\alpha}{\partial \sigma_\beta} - \frac{\partial \hat{\mathcal{H}}_\beta}{\partial \sigma_\alpha} + [\hat{\mathcal{H}}_\alpha, \hat{\mathcal{H}}_\beta]. \quad (2.13)$$

When pulled back to the vector representation of $\mathfrak{se}(2)$, the curvature field \mathcal{F} has three components, $\mathcal{F} = (\mathcal{F}_x, \mathcal{F}_y, \mathcal{F}_\theta)^T$, which can be interpreted as the effect of small loop gaits on each spatial direction according to Stokes' theorem. Finally, according to the Ambrose–Singer theorem (Ambrose & Singer 1953), we have (Shapere & Wilczek 1989)

$$\bar{\mathbf{P}} \exp \left[\int_0^T \hat{\mathcal{A}}(t) dt \right] \approx 1 + \frac{1}{2} \sum_{\alpha, \beta} \int_0^T \hat{\mathcal{F}}_{\alpha\beta} \sigma_\alpha \dot{\sigma}_\beta dt, \quad (2.14)$$

up to the second order of amplitude.

2.2. Locomotion with isotropic drag

In this subsection, we focus on the particular case of isotropic drag, i.e. $\gamma = 1$. Note that the arguments below are not limited to planar motion, but are valid for general three-dimensional motion without external forces and torques.

Isotropic drag has been known to hinder locomotion. The classical RFT study by Gray & Hancock (1955) considered simple sinusoidal transverse deformation, and theoretically showed that drag anisotropy allows net locomotion. Becker, Koehler & Stone (2003) later extended this argument to a general self-propelled free-swimming slender object, and showed that no net motion is possible in isotropic drag with only bending deformation. These studies, however, neglected rotational dynamics; it was then proven that isotropic drag may be compatible with net rotation (Koens & Lauga 2016). Finally, considering extensible slender swimmers, Pak & Lauga (2011) argued that time variation of the total length can generate net locomotion in isotropic drag.

However, ambiguity remains regarding the need for total length variation, and the exact role played by compression in allowing locomotion in isotropic drag. Here, we answer precisely with the proposition below.

PROPOSITION 1. *Assume that $\gamma = 1$. Let $\bar{\mathbf{X}}$ be the centre of geometry of the swimmer, defined as*

$$\bar{\mathbf{X}}(t) = \frac{1}{L} \int_0^{L(t)} \mathbf{x}(s, t) ds. \quad (2.15)$$

Then the following statements hold:

- (i) *If the compression is spatially uniform ($\partial p / \partial s_0 = 0$ for all times), then $\dot{\bar{\mathbf{X}}} = 0$, i.e. no net motion is possible.*
- (ii) *Otherwise ($\partial p / \partial s_0 \neq 0$), net motion is indeed possible.*

Of particular note, case (ii) includes the case $\dot{L} = 0$ of constant total length, contrary to the statement by Pak & Lauga (2011), which restrictively assumed that the arc length s is a materially conserved quantity. This, however, is not always the case for active compression, as seen in the proof of Proposition 1 below.

Proof of Proposition 1. Let us compute the time derivative of $\bar{\mathbf{X}}$, recalling that the arc length s is provided as a function of the Lagrangian label s_0 as $s = s(s_0, t)$, which yields

the following change of variable in the integral (2.15):

$$\frac{d\bar{\mathbf{X}}}{dt} = \frac{d}{dt} \left[\frac{1}{L} \int_0^{L_0} \mathbf{x}(s_0, t) (1 + \eta p(s_0, t)) ds_0 \right], \quad (2.16)$$

where L_0 is the body length in the reference frame. The right-hand side of (2.16) is then computed as

$$-\frac{\dot{L}}{L^2} \int_0^L \mathbf{x}(s, t) ds + \frac{1}{L} \int_0^{L_0} \frac{\partial \mathbf{x}(s_0, t)}{\partial t} (1 + \eta p) ds_0 + \frac{\eta}{L} \int_0^{L_0} \mathbf{x}(s_0, t) \frac{\partial p}{\partial t} ds_0. \quad (2.17)$$

Assuming isotropic drag ($C_{\parallel} = C_{\perp} = C$), the second term vanishes, because one has

$$\int_0^{L_0} \frac{\partial \mathbf{x}(s_0, t)}{\partial t} (1 + \eta p(s_0, t)) ds_0 = \int_0^L \frac{D\mathbf{x}}{Dt} ds = \frac{1}{C} \int_0^L \mathbf{f} ds = \mathbf{0} \quad (2.18)$$

from the force balance equations (2.4) and (2.5). By writing \dot{L} as

$$\frac{dL}{dt} = \frac{d}{dt} \int_0^{L_0} [1 + \eta p(s_0, t)] ds_0 = \eta \int_0^{L_0} \frac{\partial p(s_0, t)}{\partial t} ds_0, \quad (2.19)$$

we may summarise the motion of the centre of geometry in the isotropic drag case as

$$\frac{d\bar{\mathbf{X}}}{dt} = \frac{\eta}{L} \left[\int_0^{L_0} \left(\mathbf{x}(s_0, t) \frac{\partial p(s_0, t)}{\partial t} \right) ds_0 - \bar{\mathbf{X}} \int_0^{L_0} \frac{\partial p(s_0, t)}{\partial t} ds_0 \right], \quad (2.20)$$

which is clearly non-zero in general, hence point (ii) of the proposition. Note that we can also recover, from (2.20), the zero motion for an inextensible object, by setting $\eta = 0$.

Now we assume uniform compression, i.e. $\partial p / \partial s_0 = 0$, so $\partial p(s_0, t) / \partial t = \dot{p}$. Equation (2.20) then becomes

$$\frac{d\bar{\mathbf{X}}}{dt} = \frac{\eta \dot{p}}{L} \left[\int_0^{L_0} \mathbf{x}(s_0, t) ds_0 - L_0 \bar{\mathbf{X}} \right] = \frac{\eta \dot{p}}{L} \left[\frac{L_0}{L} \int_0^{L_0} \mathbf{x}(s_0, t) (1 + \eta p) ds_0 - L_0 \bar{\mathbf{X}} \right] = \mathbf{0}, \quad (2.21)$$

which proves point (i). \square

The first term on the right-hand side of (2.20) clearly highlights how the coupling between the local position and the compression rate contributes to the net motion, and this means in particular that a change of total length is not essential for the generation of motion. In the following sections, we quantitatively investigate the role of this coupling.

3. Minimal model of swimming with bending-compression coupling

In order to illustrate the statement of Proposition 1 and explore further how locomotion can result from the coupling between curvature-type and compression-type degrees of freedom, we first consider a minimal model, made of two rigid links connected by a hinge (figure 2). In this minimal model, compression is materialised by a uniformly distributed variation of the lengths of the links, while bending is represented by the varying angle between the links. Here, we consider an additional relationship between the lengths of the two links in order to retain only one independent parameter for compression; then we obtain a system with two shape variables ($N = 2$ in the previous section): one angle for bending, and one length ratio for compression.

If we further forbid compression, then the model becomes the so-called ‘scallop’, which famously cannot swim (Purcell 1977); it is often used as an illustration of the fact that in inertialess environments, at least two degrees of freedom are necessary for a deformation

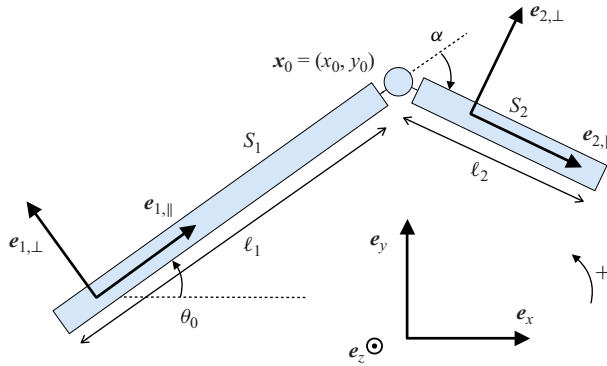


Figure 2. Set-up and notations for the minimal model.

cycle to result in net locomotion, which can be seen from the connection structure in (2.10). In turn, several studies have proposed minimal models with a second degree of freedom, whether it is angular (‘Purcell swimmer’) (Purcell 1977; Moreau 2019; Ishimoto, Moreau & Yasuda 2022), linear (‘three-sphere swimmer’) (Najafi & Golestanian 2004; Yasuda, Hosaka & Komura 2023) or volumic (‘push-me-pull-you swimmer’) (Avron, Kenneth & Oaknin 2005; Silverberg *et al.* 2020).

In this section, we add to this family what we could playfully call a ‘squeeze-me-bend-you swimmer’, with compression as a second degree of freedom. A similar model has been studied in Gidoni *et al.* (2024), with a comparison between different distributions of compression along each link (i.e. the function $p(s_0, t)$), and focusing on model controllability with a limited range of γ . Beyond controllability, the simplicity of the model allows analytical computation of the Stokes connection and curvature fields, which we use here to gain intuition of the locomotion capabilities offered by bending–compression coupling, and propose elementary gaits.

3.1. Model

We consider an idealised planar swimmer made of two rigid slender rods S_1, S_2 of lengths ℓ_1, ℓ_2 , connected by a junction, and assume that the swimmer is situated in an $x-y$ plane. The position of the swimmer with respect to the fixed frame $(\mathbf{e}_x, \mathbf{e}_y, \mathbf{e}_z)$ is represented by the position of the junction between the two rods, and is denoted by $\mathbf{x}_0 = (x_0, y_0)$. Additionally, we consider two moving frames $(\mathbf{e}_{1,\parallel}, \mathbf{e}_{1,\perp})$ and $(\mathbf{e}_{2,\parallel}, \mathbf{e}_{2,\perp})$ attached to each rod. We denote by θ_0 the angle between \mathbf{e}_x and $\mathbf{e}_{1,\parallel}$, and by α the angle between $\mathbf{e}_{1,\parallel}$ and $\mathbf{e}_{2,\parallel}$. These angles are taken positive for an anticlockwise rotation from \mathbf{e}_x and $\mathbf{e}_{1,\parallel}$, respectively.

Here, we assume that the angle α and the lengths ℓ_1, ℓ_2 evolve in time according to some prescribed gait, and aim to derive the effect of such a gait on the swimmer configuration in space: position \mathbf{x}_0 and orientation θ . To track the current length of segment S_i with respect to its reference length ℓ_i^0 , we introduce β_i such that $\ell_i = \beta_i \ell_i^0$.

In particular, we focus on two subcases of interest for the compression. The first case is uniform compression. Unicellular swimming microorganisms such as *Stentor* and *Lacrymaria* exhibit morphological changes of their helically coiled structure during the compression and extensions, and it is reasonable to assume uniform compression/extension as a simple model of their deformation. In the two-link model, this means $\ell_1 = \ell_2$ at all times, or

$$\beta_2 = \frac{\ell_1^0}{\ell_2^0} \beta_1, \quad (3.1)$$

which yields $\beta_1 = \beta_2$ at all times if $\ell_1^0 = \ell_2^0$.

The second subcase is the constant total length, which fits case (ii) of Proposition 1 and may model distributed muscular contraction. In the two-link model, it translates as $\ell_1 + \ell_2 = \ell_1^0 + \ell_2^0$ at all times, or

$$\beta_2 = \left(1 + \frac{\ell_1^0}{\ell_2^0}\right) - \frac{\ell_1^0}{\ell_2^0} \beta_1, \quad (3.2)$$

which means $\beta_1 + \beta_2 = 2$ at all times if $\ell_1^0 = \ell_2^0$.

For $s_0 \in [0, \ell_i^0]$, let $\mathbf{x}_i(s_0)$ be the coordinates of the point of Lagrangian label s_0 on segment i , with the origin of coordinates being taken at the $S_1 - S_2$ junction. Then it holds that

$$\mathbf{x}_1(s_0) = \mathbf{x}_0 - s_0 \beta_1 \mathbf{e}_{1,\parallel}, \quad (3.3)$$

$$\mathbf{x}_2(s_0) = \mathbf{x}_0 + s_0 \beta_2 \mathbf{e}_{2,\parallel}, \quad (3.4)$$

and it follows, for the local velocity at $\mathbf{x}_i(s_0)$, that

$$\dot{\mathbf{x}}_1(s_0) = \dot{\mathbf{x}}_0 - s_0 \dot{\beta}_1 \mathbf{e}_{1,\parallel} - s_0 \beta_1 \dot{\theta} \mathbf{e}_{1,\perp}, \quad (3.5)$$

$$\dot{\mathbf{x}}_2(s_0) = \dot{\mathbf{x}}_0 + s_0 \dot{\beta}_2 \mathbf{e}_{2,\parallel} + s_0 \beta_2 (\dot{\theta} + \dot{\alpha}) \mathbf{e}_{2,\perp}. \quad (3.6)$$

Using (2.4), we can express the local force density exerted by the fluid on the swimmer at point $\mathbf{x}_i(s_0)$:

$$\mathbf{f}_i(s_0) = -C_{\parallel} (\dot{\mathbf{x}}_i \cdot \mathbf{e}_{\parallel}) \mathbf{e}_{\parallel} - C_{\perp} (\dot{\mathbf{x}}_i \cdot \mathbf{e}_{\perp}) \mathbf{e}_{\perp}. \quad (3.7)$$

Then one can compute the total hydrodynamic force on each segment, scaled by extension β_i :

$$\mathbf{F}_i = \int_{S_i} \mathbf{f}_i dS_i = \int_0^{\ell_i^0} \beta_i \mathbf{f}_i(s_0) ds_0, \quad (3.8)$$

which yields

$$\begin{aligned} \mathbf{F}_1 = & -\dot{\mathbf{x}}_0 \beta_1 \ell_1^0 (C_{\parallel} \cos \theta_0 \mathbf{e}_{1,\parallel} - C_{\perp} \sin \theta_0 \mathbf{e}_{1,\perp}) \\ & - \dot{\beta}_1 \ell_1^0 (C_{\parallel} \sin \theta_0 \mathbf{e}_{1,\parallel} + C_{\perp} \cos \theta_0 \mathbf{e}_{1,\perp}) \\ & + \dot{\theta}_0 C_{\perp} \beta_1^2 \frac{(\ell_1^0)^2}{2} \mathbf{e}_{1,\perp} + C_{\parallel} \beta_1 \dot{\beta}_1 \frac{(\ell_1^0)^2}{2} \mathbf{e}_{1,\parallel}, \end{aligned} \quad (3.9)$$

$$\begin{aligned} \mathbf{F}_2 = & -\dot{\mathbf{x}}_0 \beta_2 \ell_2^0 (C_{\parallel} \cos(\theta_0 + \alpha) \mathbf{e}_{2,\parallel} - C_{\perp} \sin(\theta_0 + \alpha) \mathbf{e}_{2,\perp}) \\ & - \dot{\beta}_2 \ell_2^0 (C_{\parallel} \sin(\theta_0 + \alpha) \mathbf{e}_{2,\parallel} + C_{\perp} \cos(\theta_0 + \alpha) \mathbf{e}_{2,\perp}) \\ & + (\dot{\theta}_0 + \dot{\alpha}) C_{\perp} \beta_2^2 \frac{(\ell_2^0)^2}{2} \mathbf{e}_{2,\perp} + C_{\parallel} \beta_2 \dot{\beta}_2 \frac{(\ell_2^0)^2}{2} \mathbf{e}_{2,\parallel}. \end{aligned} \quad (3.10)$$

Similarly, the torques T_1 and T_2 on each segment with respect to the junction point, and projected on \mathbf{e}_z , are given by

$$T_1 = \beta_1^2 C_{\perp} \frac{(\ell_1^0)^2}{2} (-\dot{x}_0 \cos \theta_0 + \dot{y}_0 \sin \theta_0) + \dot{\theta}_0 \beta_1^3 \frac{(\ell_1^0)^3}{3}, \quad (3.11)$$

$$T_2 = \beta_2^2 C_{\perp} \frac{(\ell_2^0)^2}{2} (\dot{x}_0 \cos(\theta_0 + \alpha) + \dot{y}_0 \sin(\theta_0 + \alpha)) + (\dot{\theta}_0 + \dot{\alpha}) \beta_2^3 \frac{(\ell_2^0)^3}{3}. \quad (3.12)$$

Since inertia is negligible, we can write balance of force and torques at all times:

$$\begin{cases} \mathbf{F}_1 + \mathbf{F}_2 = 0, \\ T_1 + T_2 = 0. \end{cases} \quad (3.13)$$

Using (3.9)–(3.13), and plugging the expression for β_2 with respect to β_1 , one can derive the Stokes connection that links shape velocities $(\dot{\alpha}, \dot{\beta}_1)$ to rigid motion velocities in the reference frame $(\dot{x}_0, \dot{y}_0, \dot{\theta}_0)$:

$$\mathbf{A}(\theta_0, \alpha, \beta_1) \begin{pmatrix} \dot{x}_0 \\ \dot{y}_0 \\ \dot{\theta}_0 \end{pmatrix} = \mathbf{B}(\theta_0, \alpha, \beta_1) \begin{pmatrix} \dot{\alpha} \\ \dot{\beta}_1 \end{pmatrix}. \quad (3.14)$$

To highlight the existence of a connection, we rewrite the resistance matrices in a moving frame $(\mathbf{e}_{a,\parallel}, \mathbf{e}_{a,\perp})$ representing the average orientation of the swimmer, namely at $\theta_0 + \alpha/2$. As noted by Hatton & Choset (2015) and Bass, Ramasamy & Hatton (2022), this frame has the important advantage of minimising the error accumulated by higher-order terms when integrating the Stokes curvature (2.10) over a loop trajectory in the shape space. Hence we define $\mathbf{A}_a = \mathbf{R}_{\theta_0+\alpha/2}^{-1} \mathbf{A} \mathbf{R}_{\theta_0+\alpha/2}$ and $\mathbf{B}_a = \mathbf{R}_{\theta_0+\alpha/2}^{-1} \mathbf{B}$, and write (3.14) in the form,

$$\mathbf{R}_{\theta_0+\alpha/2}^{-1} \begin{pmatrix} \dot{x}_0 \\ \dot{y}_0 \\ \dot{\theta}_0 \end{pmatrix} = \mathcal{H} \begin{pmatrix} \dot{\alpha} \\ \dot{\beta}_1 \end{pmatrix}, \quad (3.15)$$

where the connection \mathcal{H} is given by $\mathcal{H} = \mathbf{A}_a^{-1} \mathbf{B}_a$.

Now let us give detailed expressions of these matrices in both cases of interest, (3.1) and (3.2). For simplicity, we assume $\ell_1^0 = \ell_2^0 = \ell$. In the case of uniform compression (3.1), one obtains

$$\mathcal{H} = \begin{pmatrix} 0 & 0 \\ -\frac{\beta_1 \gamma \ell \cos\left(\frac{\alpha}{2}\right)}{4\left[1 + (\gamma - 1) \cos^2\left(\frac{\alpha}{2}\right)\right]} & \frac{\ell \sin\left(\frac{\alpha}{2}\right)}{2\left[\gamma + (1 - \gamma) \sin^2\left(\frac{\alpha}{2}\right)\right]} \\ -1/2 & 0 \end{pmatrix}. \quad (3.16)$$

Then one can compute the velocity of the geometric centre from its definition as $\mathbf{x}_m = (1/4)(2\mathbf{x}_0 + \mathbf{x}_1(\ell) + \mathbf{x}_2(\ell))$, which, expressed in the rotating basis $(\mathbf{e}_{a,\parallel}, \mathbf{e}_{a,\perp})$, yields the motion only in the y_m direction, with its velocity given by

$$\dot{y}_m = \frac{\ell \cos\left(\frac{\alpha}{2}\right) (\gamma - 1) \left[\beta_1 \sin \alpha + \frac{\alpha \beta_1}{2} (\cos \alpha - 1) \right]}{2\gamma - 2 \cos \alpha + 2\gamma \cos \alpha + 2}, \quad (3.17)$$

from which we deduce that any translational motion occurs along the y_m direction. Moreover, it is clear that isotropic drag ($\gamma = 1$) forbids any translation, in agreement with case (i) of Proposition 1.

In the case of constant total length (3.2), one has

$$\mathbf{A}_a = \begin{pmatrix} \ell(\gamma + \cos \alpha - \gamma \cos \alpha + 1) & \ell \sin \alpha (\beta_1 - 1)(\gamma - 1) & -\gamma \ell^2 \sin(\alpha/2) (\beta_1^2 - 2\beta_1 + 2) \\ \ell \sin \alpha (\beta_1 - 1)(\gamma - 1) & \ell(\gamma - \cos \alpha + \gamma \cos \alpha + 1) & -2\gamma \ell^2 \cos(\alpha/2) (\beta_1 - 1) \\ -\gamma \ell^2 \sin(\alpha/2) (\beta_1^2 - 2\beta_1 + 2) & -2\gamma \ell^2 \cos(\alpha/2) (\beta_1 - 1) & -(2/3)\gamma \ell^3 (3\beta_1^2 - 6\beta_1 + 4) \end{pmatrix}, \quad (3.18)$$

and

$$\mathbf{B}_a = \begin{pmatrix} -(\gamma/2)\ell^2 \sin(\alpha/2) (\beta_1 - 2)^2 & \ell^2 \cos(\alpha/2) \\ (\gamma/2)\ell^2 \cos(\alpha/2) (\beta_1 - 2)^2 & -\ell^2 \sin(\alpha/2) (\beta_1 - 1) \\ (\gamma/3) \ell^3 (\beta_1 - 2)^3 & 0 \end{pmatrix}, \quad (3.19)$$

leading to the connection $\mathcal{H} = \mathbf{A}_a^{-1} \mathbf{B}_a$ in the form

$$\mathcal{H} = \frac{1}{Q(\cos \alpha)} \begin{pmatrix} 2\gamma \ell \beta_1^2 (\beta_1 - 2)^2 (\beta_1 - 1) \sin(\alpha/2) P_{11}(\alpha) & \ell \cos(\alpha/2) P_{12}(\alpha) \\ \gamma \ell \beta_1^2 (\beta_1 - 2)^2 \cos(\alpha/2) P_{21}(\alpha) & \gamma \ell (\beta_1 - 1) \sin(\alpha/2) P_{22}(\alpha) \\ (\beta_1 - 2)^2 P_{31}(\alpha) & \beta_1 (\beta_1 - 2) P_{32}(\alpha) \end{pmatrix}, \quad (3.20)$$

where P_{ij} are polynomials in $\cos \alpha$, $\sin \alpha$, β_1 (whose expressions are too lengthy to write fully) and γ , and Q is defined as

$$\begin{aligned} Q(x) = & \ell^4 [3\beta_1^4 (7\gamma^2 x^2 - 7\gamma^2 - 11\gamma x^2 - 2\gamma x + 13\gamma + 4x^2 - 4) \\ & + 12\beta_1^3 (-7\gamma^2 x^2 + 7\gamma^2 + 11\gamma x^2 + 2\gamma x - 13\gamma - 4x^2 + 4) \\ & + 16\beta_1^2 (7\gamma^2 x^2 - 7\gamma^2 - 11\gamma x^2 - \frac{3}{2}\gamma x + \frac{37}{2}\gamma + 4x^2 - 4) \\ & + 8\beta_1 (-7\gamma^2 x^2 + 7\gamma^2 + 11\gamma x^2 - 35\gamma - 4x^2 + 4) + 112\gamma]. \end{aligned} \quad (3.21)$$

The expression for the motion of the geometric centre can be calculated with symbolic calculus software but is too tedious to be reproduced here, even in the particular case of isotropic drag. We can, however, evaluate it at specific shapes in the case $\gamma = 1$ to ensure that motion is indeed possible. For isotropic drag ($\gamma = 1$) and flat shape ($\alpha = 0$, $\theta_0 = 0$), one obtains

$$\dot{x}_m = \frac{\ell}{2} \dot{\beta}_1, \quad \dot{y}_m = -\frac{7\beta_1 \ell (\beta_1 - 1)^2 (\beta_1 - 2)}{48\beta_1^2 - 96\beta_1 + 56} \dot{\alpha}, \quad (3.22)$$

and for links of equal length ($\beta_1 = 1$), one obtains

$$\dot{x}_m = \frac{\ell \cos(\alpha + \theta_0)}{2} \dot{\beta}_1, \quad \dot{y}_m = \frac{\ell \sin(\alpha + \theta_0)}{2} \dot{\beta}_1. \quad (3.23)$$

In both cases, it is clear that the geometric centre does not stay fixed, despite the total length of the swimmer remaining constant. This simple example therefore provides a constructive proof for point (ii) of Proposition 1.

3.2. Gait prediction

From the expression of the connection, one may obtain the curvature of the gauge field \mathcal{F} following (2.13). Since the squeeze-me-bend-you swimmer possesses only two degrees of freedom, each scalar component of \mathcal{F} can be easily visualised on a two-dimensional plane (α , β). Moreover, any deformation gait can be represented in the same plane, and (2.10) indicates that the net locomotion produced by the gait will be, at first order, proportional to \mathcal{F} integrated over the (algebraic) area enclosed by the gait cycle in the shape space. In the following, we use this principle to design simple gaits achieving elementary motion in each available direction, demonstrating the swimming capabilities of the squeeze-me-bend-you swimmer model.

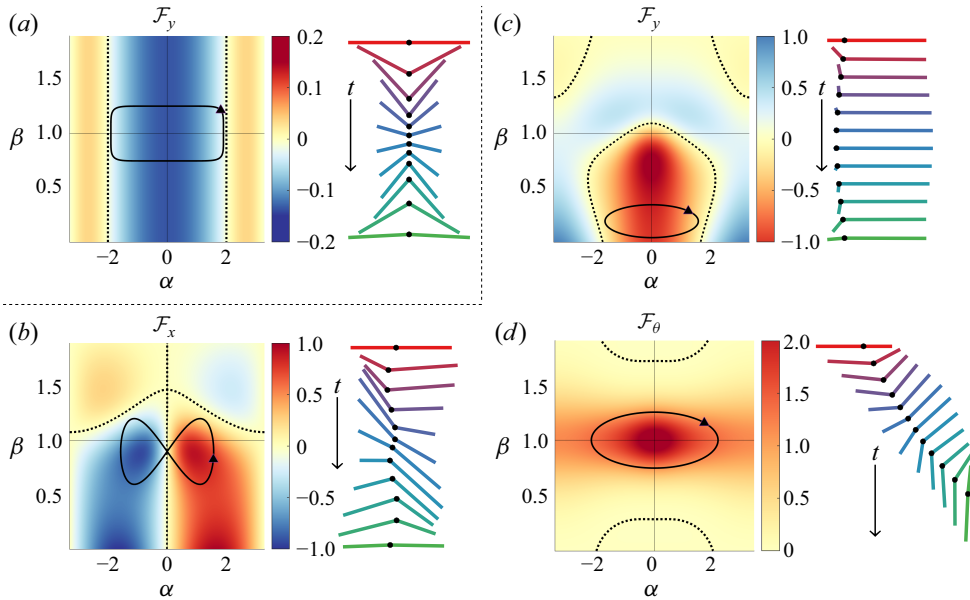


Figure 3. Curvature fields for the squeeze-me-bend-you swimmer, as defined in (2.13). Dotted black lines indicate zero-curvature level set. Suggested gaits are indicated by a continuous black line, and the corresponding deformation sequence of the swimmer is represented on the right of each curvature plot: (a) y -displacement for uniform compression, (b) x -displacement, (c) y -displacement, and (d) θ -displacement, with time progress shown by the arrow and colours.

We first examine the uniform compression case, in which only the y component of \mathcal{F} does not vanish, and takes a remarkably simple form depending only on α (and notably not on β):

$$\mathcal{F}_y = \frac{\cos\left(\frac{\alpha}{2}\right) - 3\cos\left(\frac{\alpha}{2}\right)^3}{\left(2\cos\left(\frac{\alpha}{2}\right)^2 + 2\right)^2}. \quad (3.24)$$

The function \mathcal{F}_y is even and 2π -periodic. On the interval $[-\pi, \pi]$, it vanishes at $\pm\pi$ and $\pm\alpha_m$, with $\alpha_m = \arccos(-1/3)$ (which, serendipitously, happens to be the ‘tetrahedral angle’ measured between a diagonal of a cube and its adjacent edge). It is therefore of constant sign on the interval $[-\alpha_m, \alpha_m]$, suggesting that to ensure maximal displacement, the swimmer must fold between these two values, with compression β alternating between any two set values with the same periodicity in the meantime. Such a gait is represented in figure 3(a).

In the constant length case, the symbolic expression of \mathcal{F} is not nearly nice enough to be analysed in the same way, or even reproduced here. We may nonetheless evaluate it numerically, and its three components are plotted in figure 3(b–d). Then it is possible to predict the qualitative behaviour of the swimmer after some gait by leveraging the symmetries of \mathcal{F} (Shammas, Choset & Rizzi 2007), as is classically done in analogous studies on minimal swimmer models such as the Purcell swimmer (Avron & Raz 2008). In figure 3(b), one may first observe that \mathcal{F}_x is odd in α . For this reason, a simple circular or elliptical gait centred at $(0, 1)$ would fail to produce any net locomotion in the direction x . A good candidate for a successful gait would be a ‘butterfly’ gait as shown in figure 3(b). Note that in the meantime, no motion in y or θ would result from this butterfly gait, due to

the even parity in α of \mathcal{F}_y and \mathcal{F}_θ visible in [figure 3\(c,d\)](#). On the other hand, to generate net motion purely in the y direction, an elliptical gait centred at $\alpha = 0$ may be considered, but needs to be shifted away from $\beta = 1$ to avoid producing net rotation at the same time, as shown in [figure 3\(b\)](#).

As one can infer from \mathcal{F}_θ in [figure 3\(d\)](#), elliptical gaits centred at $(0, 1)$ will rotate the swimmer in the reference plane. We note that the net rotation after one cycle is outstandingly high when compared to the capabilities of its cousin in the family of minimal swimmer models, the Purcell swimmer, which features only bending and no compression. Indeed, under the reasonable assumption that $\alpha \in [-\pi, \pi]$, a simple optimisation routine on elliptical gaits shows that the Purcell swimmer can reach a net rotation of around $\pi/2$ rad in one cycle, at most, while the squeeze-me-bend-you swimmer can achieve a rotation of nearly $3\pi/2$. This high orientational manoeuvrability suggests that compression, even in a small amount, plays a prominent role in the orientational dynamics of slender swimmers. We further quantitatively evaluate this enhancement of manoeuvrability in [§ 7](#).

4. Small-amplitude theory

In this section, we go back to a general slender object, but with a particular focus on a small bending and compression regime in order to quantify the effects of bending–compression coupling on the locomotion at low Reynolds number, by assuming $\epsilon, \eta \ll 1$ and $\eta = O(\epsilon)$.

The position in the body-fixed frame is then expanded such that

$$\begin{aligned}\tilde{x}(s_0, t) &= \int_0^{s_0} \cos(\theta(s'_0, t))(1 + \eta p(s'_0, t)) \, ds'_0 \\ &= s_0 + \eta \int_0^{s_0} p(s'_0, t) \, ds'_0 - \frac{\epsilon^2}{2} \int_0^{s_0} q^2(s'_0, t) \, ds'_0 + O(\epsilon^2 \eta),\end{aligned}\quad (4.1)$$

$$\begin{aligned}\tilde{y}(s_0, t) &= \int_0^{s_0} \sin(\theta(s'_0, t))(1 + \eta p(s'_0, t)) \, ds'_0 \\ &= \epsilon \int_0^{s_0} q(s'_0, t) [1 + \eta p(s'_0, t)] \, ds'_0 + O(\epsilon^3).\end{aligned}\quad (4.2)$$

Also, the local tangent and normal vectors need to be expanded as

$$\mathbf{e}_\parallel(s_0, t) = (1, \epsilon q)^T + O(\epsilon^2) \quad \text{and} \quad \mathbf{e}_\perp(s_0, t) = (-\epsilon q, 1)^T + O(\epsilon^2). \quad (4.3)$$

By plugging [\(4.1\)–\(4.2\)](#) into [\(2.3\)](#), we have the deformation velocity as

$$\frac{D\tilde{x}}{Dt} = \frac{\partial \tilde{x}}{\partial t}(s_0, t) = \eta \int_0^{s_0} \frac{\partial p}{\partial t}(s'_0, t) \, ds'_0 - \frac{\epsilon^2}{2} \int_0^{s_0} \frac{\partial q^2(s'_0, t)}{\partial t} \, ds'_0 + O(\epsilon^2 \eta), \quad (4.4)$$

$$\frac{D\tilde{y}}{Dt} = \frac{\partial \tilde{y}}{\partial t}(s_0, t) = \epsilon \int_0^{s_0} \frac{\partial}{\partial t} [q(s'_0, t) (1 + \eta p(s'_0, t))] \, ds'_0 + O(\epsilon^2), \quad (4.5)$$

noting that the perpendicular deformation velocity contains both the bending and the compression.

We consider expansions with respect to the small parameters ϵ and η for the velocities in the body-fixed frame and rotational velocity. With the velocities in the body-fixed frame written as $\tilde{\mathbf{U}} = (\tilde{U}_x, \tilde{U}_y)^T$, i.e. $\mathbf{U} = \mathbf{R}_\theta \tilde{\mathbf{U}}$, we use the following notations for the expansions:

$$\tilde{U}_x = \tilde{U}_x^{(1)} + \tilde{U}_x^{(2)} + \tilde{U}_x^{(3)} + \dots, \quad (4.6)$$

$$\tilde{U}_y = \tilde{U}_y^{(1)} + \tilde{U}_y^{(2)} + \tilde{U}_y^{(3)} + \dots, \quad (4.7)$$

$$\Omega = \Omega^{(1)} + \Omega^{(2)} + \Omega^{(3)} + \dots, \quad (4.8)$$

where the superscripts ⁽¹⁾, ⁽²⁾ and ⁽³⁾ indicate the linear, quadratic and cubic terms of ϵ and η , respectively.

4.1. Leading-order calculations

We first consider $\tilde{F}_x = 0$ by substituting (2.1)–(2.2) into (2.5), to obtain, up to the second order of expansions,

$$\int_0^L \left(\tilde{U}_x + \frac{D\tilde{x}}{Dt} \right) ds = \epsilon \Omega \int_0^L q \tilde{y} ds + \epsilon(\gamma - 1) \int_0^L q \left(\tilde{U}_y + \Omega \tilde{x} + \frac{D\tilde{y}}{Dt} \right) ds + O(\epsilon^3, \epsilon^2 \eta). \quad (4.9)$$

Here, we find that the right-hand side of (4.9) is of the second order of small parameters, while the left-hand side is of the first order of magnitudes. Hence at the leading order of the expansions, we have

$$\tilde{U}_x^{(1)} = -\frac{\eta}{L} \int_0^{L_0} \left[\int_0^{s_0} \frac{\partial p}{\partial t}(s'_0, t) ds'_0 \right] ds_0. \quad (4.10)$$

We then consider the force balance in the normal direction by imposing $\tilde{F}_y = 0$, which is written as

$$\epsilon(\gamma - 1) \int_0^L q \left(\tilde{U}_x + \frac{D\tilde{x}}{Dt} \right) ds = \gamma \int_0^L \left(\tilde{U}_y + \Omega \tilde{x} + \frac{D\tilde{y}}{Dt} \right) ds + O(\epsilon^3, \epsilon^2 \eta). \quad (4.11)$$

Similarly, the torque balance $\tilde{M} = 0$ reads

$$\begin{aligned} & \epsilon(\gamma - 1) \int_0^L q \tilde{x} \left(\tilde{U}_x + \frac{D\tilde{x}}{Dt} \right) ds + \int_0^L \tilde{y} \left(\tilde{U}_x + \frac{D\tilde{x}}{Dt} \right) ds \\ & = \gamma \int_0^L \tilde{x} \left(\tilde{U}_y + \Omega \tilde{x} + \frac{D\tilde{y}}{Dt} \right) ds + O(\epsilon^3, \epsilon^2 \eta). \end{aligned} \quad (4.12)$$

By similar order estimates for (4.11)–(4.12), we find that in the leading order, only the right-most integral contributes in each equation. Hence we obtain

$$L \tilde{U}_y^{(1)} + \frac{L^2}{2} \Omega^{(1)} + \epsilon \int_0^{L_0} \frac{\partial q}{\partial t}(s_0, t) ds_0 = 0, \quad (4.13)$$

$$\frac{L^2}{2} \tilde{U}_y^{(1)} + \frac{L^3}{3} \Omega^{(1)} + \epsilon \int_0^{L_0} s_0 \frac{\partial q}{\partial t}(s_0, t) ds_0 = 0, \quad (4.14)$$

yielding the first-order velocities

$$\tilde{U}_y^{(1)} = -\frac{6\epsilon}{L^2} \int_0^{L_0} \left(\frac{2L}{3} - s_0 \right) \frac{\partial q}{\partial t} ds_0, \quad (4.15)$$

$$\Omega^{(1)} = \frac{12\epsilon}{L^3} \int_0^{L_0} \left(\frac{L}{2} - s_0 \right) \frac{\partial q}{\partial t} ds_0. \quad (4.16)$$

4.2. Second-order calculations

We then proceed to the second-order velocities, by substituting the leading-order results into the force and torque balance equations (4.9)–(4.12).

We start with the tangential force balance. The second-order contributions are calculated as

$$L\tilde{U}_x^{(2)} + \int_0^L (\tilde{W}_x - \Omega^{(1)}\tilde{y}) \, ds + \epsilon(1 - \gamma) \int_0^L q \left(\tilde{U}_y^{(1)} + \Omega^{(1)}\tilde{x} + \frac{D\tilde{y}}{Dt} \right) \, ds = 0, \quad (4.17)$$

where we introduced

$$\tilde{W}_x(s_0, t) := \tilde{U}_x^{(1)} + \frac{D\tilde{x}}{Dt}. \quad (4.18)$$

From (4.17), we may readily obtain the second-order tangential velocity $\tilde{U}_x^{(2)}$. Similarly, the normal force balance and torque balance equations are expanded up to second order as

$$\epsilon(\gamma - 1) \int_0^L q \tilde{W}_x \, ds = \gamma \int_0^L \left(\tilde{U}_y^{(1)} + \Omega^{(1)}\tilde{x} + \frac{D\tilde{y}}{Dt} \right) \, ds + \gamma \left(L\tilde{U}_y^{(2)} + \frac{L^2}{2} \Omega^{(2)} \right) \quad (4.19)$$

and

$$\begin{aligned} \epsilon(\gamma - 1) \int_0^L q \tilde{x} \tilde{W}_x \, ds &= - \int_0^L \tilde{y} \tilde{W}_x \, ds + \gamma \int_0^L \tilde{x} \left(\tilde{U}_y^{(1)} + \Omega^{(1)}\tilde{x} + \frac{D\tilde{y}}{Dt} \right) \, ds \\ &\quad + \gamma \left(\frac{L^2}{2} \tilde{U}_y^{(2)} + \frac{L^3}{3} \Omega^{(2)} \right), \end{aligned} \quad (4.20)$$

respectively. Hence $\tilde{U}_y^{(2)}$ and $\Omega^{(2)}$ may be calculated by evaluating the integrals in (4.19)–(4.20) up to second order.

4.3. Third-order calculations

To obtain the third-order progressive velocity, one needs to expand the position \tilde{x} and \tilde{y} , and the vectors \mathbf{n} and \mathbf{t} , up to the third order of small parameters ϵ and η . The force balance equations in the \tilde{x} direction (4.9) are therefore evaluated as

$$\begin{aligned} \tilde{U}_x^{(3)}L - \tilde{\Omega}^{(2)} \int_0^L \tilde{y} \, ds + \int_0^L \left[\tilde{W}_x + \tilde{U}_y^{(2)} - \tilde{\Omega}^{(1)}\tilde{y} \right] \left(1 - \epsilon^2 q^2 \right) \, ds + \epsilon^2 \gamma \int_0^L q^2 \tilde{W}_x \, ds \\ + \epsilon(1 - \gamma) \int_0^L \left[\tilde{U}_y^{(1)} + \tilde{U}_y^{(2)} + (\tilde{\Omega}^{(1)} + \tilde{\Omega}^{(2)})\tilde{x} + \frac{D\tilde{y}}{Dt} \right] \, ds = 0, \end{aligned} \quad (4.21)$$

by neglecting the fourth- and higher-order terms. Since the first- and second-order velocities are all calculated, by substituting these expressions into (4.21) and evaluating the integrals, we may obtain the expression for the third-order tangential velocity $\tilde{U}_x^{(3)}$.

5. Bending wave with uniform compression

5.1. Uniform compression

As an illustrative example, we first consider locomotion with bending wave and uniform compression, given by

$$p(s_0, t) = \sin(\omega t) \quad \text{and} \quad q(s_0, t) = \sin(ks_0 + \omega t + \phi), \quad (5.1)$$

where $\phi \in [0, 2\pi)$ denotes the phase difference between the two modes. For simplicity, we assume that the filament contains an integer number of waves, i.e. $kL_0 = \pm 2\pi, \pm 4\pi, \pm 6\pi, \dots$

The first-order calculations provide

$$\tilde{U}_x^{(1)} = -\frac{\eta\omega L_0}{2} \cos \omega t, \quad (5.2)$$

$$\tilde{U}_y^{(1)} = \frac{\epsilon\omega}{k} \sin(\omega t + \phi) - \frac{6\epsilon\omega}{k^2 L_0} \cos(\omega t + \phi), \quad (5.3)$$

$$\Omega^{(1)} = \frac{12\epsilon\omega}{k^2 L_0^2} \cos(\omega t + \phi), \quad (5.4)$$

which vanish after averaging over a time period.

We then proceed to calculating the second-order contributions. The tangential velocity at the second order may be calculated from (4.17) as

$$\tilde{U}_x^{(2)} = \frac{\epsilon^2\omega}{2k} \left[(\gamma - 1) + \frac{1}{2} \cos(2\omega t + 2\phi) \right] - \frac{6\epsilon^2\omega}{k^3 L_0^2} (\gamma - 2) [1 + \cos(2\omega t + 2\phi)]. \quad (5.5)$$

By calculating the integrals and solving the linear problem at the second-order equations (4.19)–(4.20), we obtain

$$\begin{aligned} \tilde{U}_y^{(2)} = & -\frac{\epsilon\eta\omega}{2k} \left[\left(\frac{\gamma - 1}{\gamma} \right) \cos \phi + \left(\frac{3\gamma - 1}{\gamma} \right) \cos(2\omega t + \phi) \right] \\ & - \frac{3\epsilon\eta\omega}{k^2 L_0^3} \left[\left(\frac{2\gamma - 3}{\gamma} \right) \sin \phi + \left(\frac{4\gamma - 3}{\gamma} \right) \sin(2\omega t + \phi) \right] \end{aligned} \quad (5.6)$$

$$\Omega^{(2)} = \frac{18\epsilon\eta\omega}{k^2 L_0^2} \left(\frac{\gamma - 1}{\gamma} \right) [\sin \phi + \sin(2\omega t + \phi)]. \quad (5.7)$$

By taking the time average, we have

$$\langle \tilde{U}_x \rangle = \frac{\epsilon^2\omega}{2k} (\gamma - 1) - \frac{6\epsilon^2\omega}{k^3 L_0^2} (\gamma - 2), \quad (5.8)$$

$$\langle \tilde{U}_y \rangle = -\frac{\epsilon\eta\omega}{2k} \left(\frac{\gamma - 1}{\gamma} \right) \cos \phi - \frac{3\epsilon\eta\omega}{k^2 L_0} \left(\frac{2\gamma - 3}{\gamma} \right) \sin \phi, \quad (5.9)$$

and for the angular velocity,

$$\langle \Omega \rangle = \frac{18\epsilon\eta\omega}{k^2 L_0^2} \left(\frac{\gamma - 1}{\gamma} \right) \sin \phi, \quad (5.10)$$

where we introduced the time average symbol, $\langle \bullet \rangle = (1/T) \int_0^T \bullet dt$, and deformation time period $T = 2\pi/\omega$. To obtain the expressions in the laboratory frame to second order, one needs to take the non-commutative effects into account as in (2.9). Instead of using the gauge-theoretical method, we directly compute the Magnus expansion (2.9), as the shape variable is not obvious in the continuous filament model. The final results are then obtained as

$$\langle U_x \rangle = \frac{\epsilon^2\omega}{2k} (\gamma - 1) - \frac{6\epsilon^2\omega}{k^3 L_0^2} (\gamma - 1), \quad (5.11)$$

$$\langle U_y \rangle = -\frac{\epsilon\eta\omega}{2k} \left(\frac{\gamma - 1}{\gamma} \right) \cos \phi + \frac{9\epsilon\eta\omega}{k^2 L_0} \left(\frac{\gamma - 1}{\gamma} \right) \sin \phi, \quad (5.12)$$

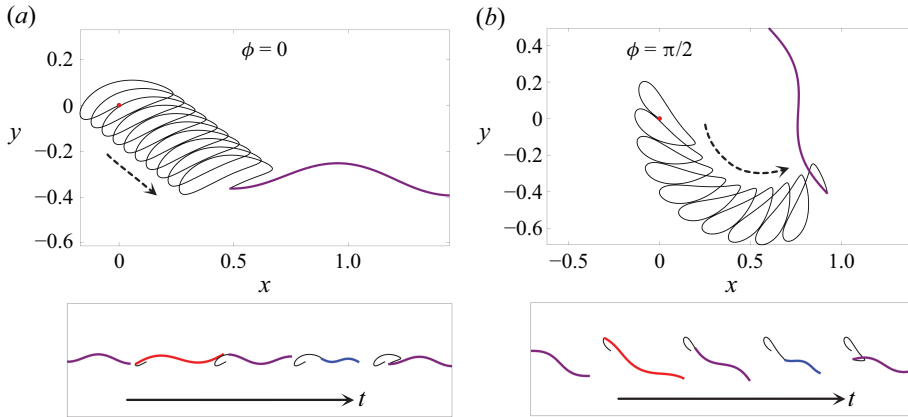


Figure 4. Top: sample trajectories of a swimmer under uniform compression with different phase shifts, (a) $\phi = 0$ and (b) $\phi = \pi/2$. The parameters are $\epsilon = \eta = 0.4$, $\gamma = 2$, $L_0 = 1$, $kL_0 = 2\pi$ and $\omega = 1$. With the initial position $(0, 0)$ (marked by a red dot) and the initial angle $\theta = 0$, we drew the orbits of the leftmost end of the filament from $t = 0$ to $t = 10$. The configuration at $t = 10$ is also shown. Bottom: time sequence of swimmer shape from $t = 0$ to $t = 1$ with the local extension visualised by the colours.

while the rotational velocity is unchanged from (5.10). We clearly find no net locomotion with the isotropic drag ($\gamma = 1$) for the uniform compression as in the general theory in § 2.2.

The corrections by the Lie bracket appear in the second terms in (5.11)–(5.12), which represent the finite-size effect of the body, and vanish in the limit $kL \rightarrow \infty$. Many mathematical models with bending motions including the Taylor sheet and a slender filament model usually assume one-dimensional motion, while this simplification is only valid for an infinitely long body, because the instantaneous lateral and rotational motion, in general, does not vanish. This result highlights the importance of the motion non-commutativity for a finite-sized swimmer with lateral oscillation, the so-called yawing motion.

Although the compression itself does not generate progressive velocity, the bending–compression coupling in the $O(\epsilon\eta)$ terms generates both normal translation and rotation. This notably underlines the enhancement of manoeuvrability through body compression. In fact, by manipulating the phase shift ϕ , the swimmer is able to make a turn in both directions.

When $\sin \phi = 0$, as found from (5.10), no net rotation is generated. To analyse this no-net-rotation property in the large-amplitude case, we numerically examine the swimmer dynamics, by discretising the slender swimmer by N small segments with length ℓ_i ($i = 1, \dots, N$), known as the N -link model (Moreau, Giraldi & Gad  lha 2018). In the case of the current kinematic problem, we prescribe the segment length and the angle between the i th and $(i + 1)$ th segments, which we denote by α_i ($i = 1, \dots, N - 1$). The force balance and torque balances (2.5) are then computed by summing the contributions from each segment. These balance relations then form linear equations for the translational and rotational velocities. In the numerical calculations below, we use $N = 40$, which guarantees satisfying numerical accuracy for our purpose. Although the non-local hydrodynamic interactions are not negligible outside the small-amplitude regime, we use the resistive drag relation as empirical modelling, with a focus on the effects of the bending–compression coupling and the mechanical roles of drag anisotropy. Sample trajectories of the swimmer are shown with its shape gait in figure 4. The no-net-motion property still holds even outside the small-amplitude regime, as seen in figure 4(a).

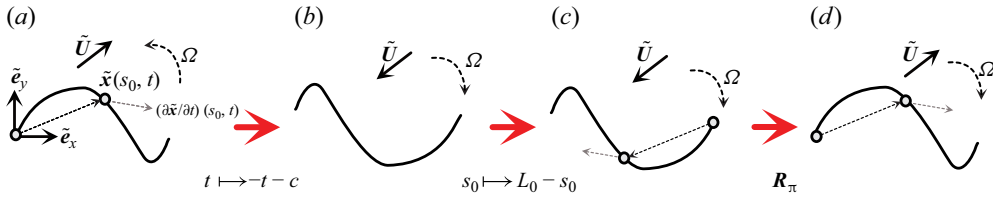


Figure 5. Schematics for the symmetry arguments of the no-net-rotation property: (a) the original shape in the body fixed frame with velocities \tilde{U} and Ω ; (b) the shape after the time reversal with a shift $c = kL_0/\omega - T/2$; (c) the head-to-tail inversion; (d) the π -rotation of the system.

In fact, this can be predicted by considerations on the symmetry of the shape gait. Let us consider two linear changes of variables: time reversal with a phase shift $t \mapsto t' = -t + T/2 + kL_0/\omega$, followed by head-to-tail inversion $s_0 \mapsto s'_0 = L_0 - s_0$ (figures 5a–c). Then the bending and compression functions are unchanged: $q(s'_0, t') = q(s_0, t)$ and $p(s'_0, t') = p(s_0, t)$, from the assumption on kL_0 . Hence the positions in the body-fixed frame also remain the same, after taking a π -rotation of the system as illustrated in figure 5(d). With this transformation of s_0 and t , the time derivatives of p and q have an additional minus sign, $\partial q'/\partial t' = -\partial q/\partial t$ and $\partial p'/\partial t' = -\partial p/\partial t$, yielding again the same shape velocity after the additional π -rotation of the system. Therefore, we recover the same shape and shape deformation velocity, while the rotation direction is reversed after the sequences of transformations (figure 5d). To compensate for the uniqueness of the motion with given boundary conditions, the net rotation must vanish, while the instantaneous rotation is still allowed by the phase shift in the transformation of t .

With $\sin \phi \neq 0$, the above symmetry arguments are no longer available. Hence, as in the case $\phi = \pi/2$ of figure 4(b), net rotational motions are generated by the bending–compression coupling, allowing the swimmer to turn.

5.2. Symmetric uniform compression

We then consider a symmetrical situation, where the functions $p(s_0, t)$ and $q(s_0, t)$ are given by

$$p(s_0, t) = \sin(2\omega t) \quad \text{and} \quad q(s_0, t) = \sin(ks_0 + \omega t + \phi), \quad (5.13)$$

to focus on progressive velocity. The assumption of an integer number of waves is again employed here.

By expanding the velocities up to second order, direct calculations then lead to the progressive velocity in the body-fixed coordinates

$$\tilde{U}_x^{(2)} = \frac{\epsilon^2 \omega}{2k} \left[(\gamma - 1) + \frac{1}{2} \cos(2\omega t + 2\phi) \right] - \frac{6\epsilon^2 \omega}{k^3 L_0^2} (\gamma - 2) [1 + \cos(2\omega t + 2\phi)], \quad (5.14)$$

as well as normal and rotational velocities

$$\begin{aligned} \tilde{U}_y^{(2)} = & -\frac{\epsilon \eta \omega}{2k} \left[\left(\frac{3\gamma - 2}{\gamma} \right) \cos(\phi - \omega t) + \left(\frac{5\gamma - 2}{\gamma} \right) \cos(3\omega t + \phi) \right] \\ & - \frac{3\epsilon \eta \omega}{k^2 L_0} \left[\left(\frac{5\gamma - 6}{\gamma} \right) \sin(\phi - \omega t) + \left(\frac{7\gamma - 6}{\gamma} \right) \sin(3\omega t + \phi) \right] \end{aligned} \quad (5.15)$$

$$\Omega^{(2)} = \frac{36\epsilon \eta \omega}{k^2 L_0^2} \left(\frac{\gamma - 1}{\gamma} \right) [\sin(\phi - \omega t) + \sin(3\omega t + \phi)]. \quad (5.16)$$

By taking the time average of the second-order velocities, we obtain

$$\langle \tilde{U}_x^{(2)} \rangle = \frac{\epsilon^2 \omega}{2k} (\gamma - 1) - \frac{6\epsilon^2 \omega}{k^3 L_0^2} (\gamma - 2), \quad (5.17)$$

and $\langle \tilde{U}_y \rangle = \langle \Omega \rangle = 0$ as expected by symmetry. After including the non-commutative effects between the normal translation and the rotation, we recover the same expression as in the asymmetrical case,

$$\langle U_x^{(2)} \rangle = \frac{\epsilon^2 \omega}{2k} (\gamma - 1) - \frac{6\epsilon^2 \omega}{k^3 L_0^2} (\gamma - 1). \quad (5.18)$$

Now let us examine the third-order contribution for the tangential velocity. We need to expand $\tilde{x}(s_0, t)$ and $\tilde{y}(s_0, t)$ as well as the vectors $\mathbf{e}_{\parallel}(s_0, t)$ and $\mathbf{e}_{\perp}(s_0, t)$ up to third orders of ϵ and η . The third-order tangential velocity in the body-fixed frame is therefore obtained by substituting the first- and second-order velocities into (4.21), and evaluating the integrals. Since the expression is lengthy, we present only the time-averaged velocity $\langle \tilde{U}_x^{(3)} \rangle$, given by

$$\langle \tilde{U}_x^{(3)} \rangle = \frac{\epsilon^2 \eta \omega}{4k} (\gamma - 1) \sin 2\phi - \frac{3\epsilon^2 \eta \omega}{k^3 L_0^2} \left(\frac{5\gamma - 6}{\gamma} \right) (\gamma - 2) \sin 2\phi. \quad (5.19)$$

We then evaluate the Lie brackets in (2.9) from the matrix $\hat{\mathcal{A}}$ by employing the first- and second-order velocities as well as $\tilde{U}_x^{(3)}$. The averaged tangential velocity in the laboratory frame may be calculated up to third order in the form $\langle U_x \rangle = \langle U_x^{(2)} \rangle + \langle U_x^{(3)} \rangle$, with

$$\langle U_x^{(3)} \rangle = \frac{\epsilon^2 \eta \omega}{4k} (\gamma - 1) \sin 2\phi - \frac{3\epsilon^2 \eta \omega}{k^3 L_0^2} \left(\frac{5\gamma - 8}{\gamma} \right) (\gamma - 1) \sin 2\phi. \quad (5.20)$$

Hence, thanks to the corrections coming from the non-commutativity of the rigid motion, we recover case (i) of Proposition 1.

The effect of uniform compression may be found at third order with an increase or decrease of velocity depending on the phase difference ϕ . We also numerically examine the effect of the uniform compression outside of the small-amplitude region, and plot the ratio of the averaged velocities with and without compression, $\langle U_x \rangle / \langle U_x |_{\eta=0} \rangle$, in figure 6. For small amplitude, we obtain that this ratio is expressed, up to third order, by a linear function of η as

$$\frac{\langle U_x \rangle}{\langle U_x |_{\eta=0} \rangle} = 1 + \frac{\langle U_x^{(3)} \rangle}{\langle U_x^{(2)} \rangle} = \frac{\eta}{2} \left(1 - \frac{15 - 24\gamma^{-1}}{k^2 L_0^2} \right) \left(1 - \frac{6}{k^2 L_0^2} \right)^{-1}. \quad (5.21)$$

As seen in the figure, the impact of the compression is linearly proportional to the compression size η , which agrees well with what the small-amplitude theory predicts. The quantitative agreements are more precise as the wavenumber k increases (see figure 6b).

Remarkably, the plots in figure 6 are only weakly affected by the size of ϵ , although the small-amplitude theory cannot apply for large ϵ .

6. Bending-compression wave

Motivated by muscular contraction, we then consider a bending-compression wave with a simple sinusoidal wave of p and q , given by

$$p(s_0, t) = \sin(ks_0 + \omega t), \quad q(s_0, t) = \sin(ks_0 + \omega t + \phi). \quad (6.1)$$

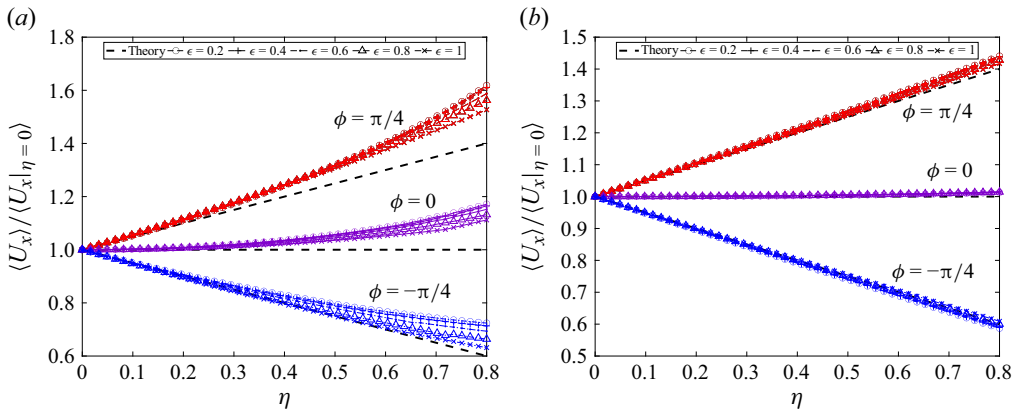


Figure 6. Impacts of uniform compression on the swimmer velocity. The averaged velocity is relative to a non-compressive bending swimmer. We used symmetrical uniform compression with $\omega = 2\pi$ and $\gamma = 2$ for different values of η and $\phi \in \{0, \pm\pi/4\}$. We used wavenumbers (a) $k = 2\pi$ and (b) $k = 6\pi$.

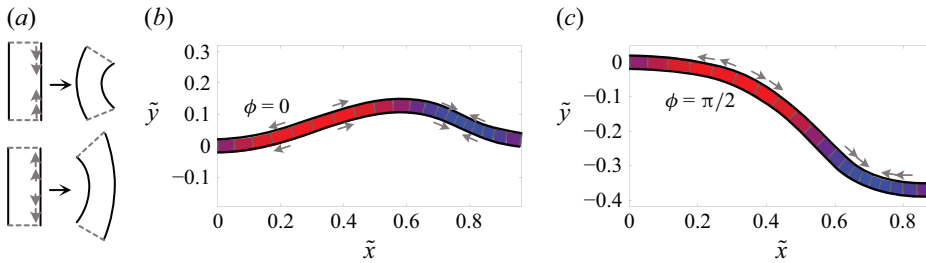


Figure 7. (a) Schematic of contraction and extension of an elastic body that exhibits bending and compression (shown by arrows). (b, c) The configuration of the swimmer with a bending-compression wave. The parameters are $\epsilon = \eta = 0.4$, $L_0 = 1$, $kL_0 = 2\pi$, $\omega = 1$, and the phase shift is chosen as (b) $\phi = 0$ and (c) $\phi = \pi/2$. We set the position as $(0, 0)$ and the initial angle as $\theta = 0$. The local extensibility of a slender body is shown by different colours, from blue (compressed) to red (extended).

As illustrated in figure 7, local contraction of one side of a slender body yields both compression and bending.

For brevity, we again assume that the filament contains an integer number of waves, i.e. $kL_0 = \pm 2\pi, \pm 4\pi, \pm 6\pi, \dots$. Also, to avoid displaying unnecessarily cumbersome expressions in the general case, we focus on two illustrative examples, $\phi = 0$ (figure 7b) and $\phi = \pi/2$ (figure 7c). This shape morphology is a counterpart example of the ‘squeeze-me-bend-you’ swimmer, with the total length L of the body remaining constant in time due to the assumption of an integer wavenumber k .

6.1. The $\phi = 0$ case

When $\phi = 0$, the compression and bending, p and q , are given by

$$p(s_0, t) = q(s_0, t) = \sin(ks_0 + \omega t). \quad (6.2)$$

An example shape of the swimmer is shown in figures 7(a) and 8(a), and the local extension $p(s_0, t)$ is visualised by the different colours from blue (compressed) to red (extended).

Using the results derived in the previous section, (4.10), (4.15) and (4.16), we readily obtain the leading-order velocities by direct calculations as

$$\tilde{U}_x^{(1)} = \frac{\eta\omega}{k} \sin \omega t, \quad (6.3)$$

$$\tilde{U}_y^{(1)} = \frac{\epsilon\omega}{k} \sin \omega t - \frac{6\epsilon\omega}{k^2 L_0} \cos \omega t, \quad (6.4)$$

$$\Omega^{(1)} = \frac{12\epsilon\omega}{k^2 L_0^2} \cos \omega t. \quad (6.5)$$

The time average of these velocities all vanish at this order, $\langle \tilde{U}_x^{(1)} \rangle = \langle \tilde{U}_y^{(1)} \rangle = \langle \Omega^{(1)} \rangle = 0$.

To examine the net locomotion, we proceed to the second-order calculations. The tangential velocity $\tilde{U}_x^{(2)}$ may be obtained by substituting the leading-order expressions into (4.17). After some manipulations, we have

$$\tilde{U}_x^{(2)} = \frac{\omega}{2k} \left[\epsilon^2(\gamma - 1) - \eta^2 + \frac{\epsilon^2}{2} \cos(2\omega t) \right] - \frac{6\omega\epsilon^2}{k^3 L_0^3} (\gamma - 2)(1 + \cos(2\omega t)). \quad (6.6)$$

From the linear equations for $\tilde{U}_y^{(2)}$ and $\Omega^{(2)}$ in (4.19)–(4.20), we may derive the second-order contributions:

$$\tilde{U}_y^{(2)} = -\frac{\epsilon\eta\omega}{2k} \left[\frac{1 + \gamma \cos(2\omega t)}{\gamma} \right] - \frac{3\epsilon\eta\omega}{2k^2 L_0} \left(\frac{\gamma + 1}{\gamma} \right) \sin(2\omega t), \quad (6.7)$$

$$\Omega^{(2)} = \frac{3\epsilon\eta\omega}{k^2 L_0^2} \left(\frac{\gamma + 1}{\gamma} \right) \sin(2\omega t). \quad (6.8)$$

To obtain the locomotion after a full deformation cycle from the instantaneous velocities, we consider the extra contribution from the non-commutative Lie algebra (see (2.9)) in addition to the time average of the velocities in the body-fixed frame, which gives

$$\langle U_x^{(2)} \rangle = \frac{\omega}{2k} [(\gamma - 1)\epsilon^2 - \eta^2] - (\gamma - 1) \frac{6\omega}{k^3 L_0^2} \epsilon^2, \quad (6.9)$$

$$\langle U_y^{(2)} \rangle = -\frac{\epsilon\eta\omega}{2\gamma k} + \frac{6\epsilon\eta\omega}{k^3 L_0^2}, \quad (6.10)$$

and the average angular velocity is simply the time average in the body-fixed frame, $\langle \Omega \rangle = 0$.

The tangential velocity $\langle U_x^{(2)} \rangle$ contains an additional compression term of $O(\eta^2)$, which remains for a purely compression/extension wave without bending. Note that the direction of swimming from the compression wave is opposite to the locomotion from the bending wave.

The normal velocity $\langle U_y^{(2)} \rangle$ does not vanish. This notable effect of the drift velocity is generated by the bending–compression coupling, seen as the $O(\epsilon\eta)$ term. The rotational motion, however, vanishes after taking the time average. To examine the dynamics outside the small-amplitude theory, we numerically solve the system and plot an example trajectory in figure 8(a). As seen in the figure, the no-net-rotation property still holds for a large amplitude, and this property is derived by the symmetry arguments as in the uniform compression case, where we consider the π -rotation of the system after the time reversal with a phase shift and the head-to-tail inversion $t \mapsto t' = -t + T/2 - kL_0/\omega$ and $s_0 \mapsto s'_0 = L_0 - s_0$ (see also figure 5). In this case, the symmetry arguments follow for any wavenumber k .

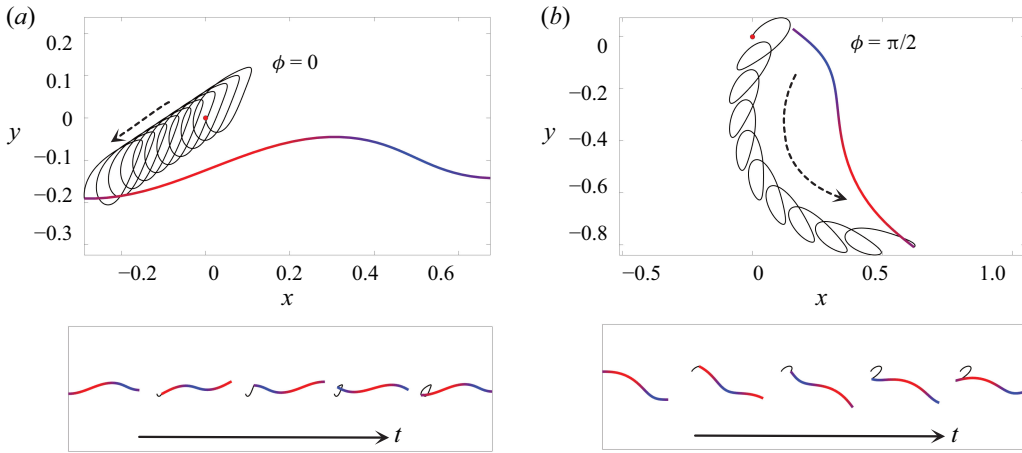


Figure 8. Top: sample trajectories of a swimmer with a bending-compression wave with (a) $\phi = 0$ and $\phi = \pi/2$. The parameters are the same as in figure 7. With the initial position $(0, 0)$ (marked by a red dot) and the initial angle $\theta = 0$, we drew the orbits of the leftmost end of the filament from $t = 0$ to $t = 10$. The configuration at $t = 10$ is also shown. Bottom: time sequence of swimmer shape from $t = 1$ to $t = 10$. The colour of the swimmer represents the local extension with the same colour as in figure 7.

6.2. The $\phi = \pi/2$ case

We then consider the situation with $\phi = \pi/2$, where the contraction of one side of the body travels down, and an example shape is shown in figures 7(b) and 8(b), with different colours illustrating the compressed (blue) and extended (red) regions.

We start with the small-amplitude regime, where we follow similar calculations as in the previous sections. By executing the calculations up to second order, and calculating the Lie brackets in (2.9), we may derive the expressions of the velocities in the laboratory frame as

$$\langle U_x^{(2)} \rangle = \frac{\omega}{2k} [(\gamma - 1)\epsilon^2 - \eta^2] - (\gamma - 1) \frac{6\omega}{k^3 L_0^2} \epsilon^2, \quad (6.11)$$

$$\langle U_y^{(2)} \rangle = -\frac{3\epsilon\eta\omega}{k^2 L_0} \left(\frac{\gamma + 1}{\gamma} \right), \quad (6.12)$$

$$\langle \Omega \rangle = \frac{6\epsilon\eta\omega}{k^2 L_0^2} \left(\frac{\gamma + 1}{\gamma} \right). \quad (6.13)$$

The velocity $\langle U_x \rangle$ has the same expression as that of the $\phi = 0$ case, while the normal and rotational velocities are qualitatively different. In particular, net rotational motion is generated. An example trajectory with its shape gait is shown in figure 7(b).

6.3. Symmetric bending-compression wave

Muscular contraction is typically generated symmetrically to avoid drifting and turning motions. In this subsection, therefore, we consider a symmetric bending-compression wave, given by

$$p(s_0, t) = \sin(ks_0 + 2\omega t) \quad \text{and} \quad q(s_0, t) = \sin(ks_0 + \omega t + \phi). \quad (6.14)$$

For brevity, we again assume that the filament contains an integer number of waves, i.e. $kL = \pm 2\pi, \pm 4\pi, \pm 6\pi, \dots$

We first consider the case with $\phi = 0$. The first-order calculations provide

$$\tilde{U}_x^{(1)} = \frac{2\eta\omega}{k} \sin(2\omega t), \quad (6.15)$$

$$\tilde{U}_y^{(1)} = \frac{\epsilon\omega}{k} \sin(\omega t) - \frac{6\epsilon\omega}{k^2 L_0} \cos(\omega t), \quad (6.16)$$

$$\Omega^{(1)} = \frac{12\epsilon\omega}{k^2 L_0^2} \cos(\omega t), \quad (6.17)$$

which yields no net motion or rotation. Up to second order, we may obtain explicit forms by estimating the integrals in (4.17) as

$$\tilde{U}_x^{(2)} = -\frac{\eta^2\omega}{k} + \frac{\epsilon^2\omega}{4k} [3 - 2\gamma - 2\cos^2\omega t] - \frac{12\epsilon^2\omega}{k^3 L_0^2} (\gamma - 2) \cos^2\omega t, \quad (6.18)$$

$$\begin{aligned} \tilde{U}_y^{(2)} = & \frac{\epsilon\eta\omega}{4k} \left[2 \left(\frac{\gamma - 2}{\gamma} \right) \cos\omega t - 3 \cos(3\omega t) \right] \\ & + \frac{\epsilon\eta\omega}{4k^2 L_0} \left[12 \left(\frac{\gamma + 1}{\gamma} \right) \sin\omega t - 3 \left(\frac{\gamma + 4}{\gamma} \right) \sin(3\omega t) \right], \end{aligned} \quad (6.19)$$

$$\Omega^{(2)} = \frac{\epsilon\eta\omega}{2} \sin\omega t + \frac{\epsilon\eta\omega}{2k^2 L_0^2} \left[6 \left(\frac{\gamma + 3}{\gamma} \right) \cos\omega t - 3 \left(\frac{3\gamma + 4}{\gamma} \right) \right] \sin\omega t. \quad (6.20)$$

By taking the time average, we derive

$$\langle \tilde{U}_x^{(2)} \rangle = \frac{\omega}{2k} [(\gamma - 1)\epsilon^2 - 2\eta^2] - \frac{6\epsilon^2\omega}{k^3 L_0^2} (\gamma - 2), \quad (6.21)$$

and zero normal and angular velocities

$$\langle \tilde{U}_y^{(2)} \rangle = 0, \quad \langle \Omega^{(2)} \rangle = 0, \quad (6.22)$$

as expected from the symmetry.

After the non-commutative algebra, the averaged velocity for the tangential velocity in the reference frame is calculated as

$$\langle U_x^{(2)} \rangle = \frac{\omega}{2k} [(\gamma - 1)\epsilon^2 - 2\eta^2] - \frac{6\epsilon^2\omega}{k^3 L_0^2} (\gamma - 1). \quad (6.23)$$

We then proceed to the third-order contributions for the progressive velocity, using (4.21) and the second-order expressions (6.18)–(6.20). Direct calculations lead to the time-averaged velocity

$$\langle \tilde{U}_x^{(3)} \rangle = \frac{3\epsilon^2\eta\omega}{2k^2 L_0^2}, \quad (6.24)$$

which is, however, found to be cancelled out in the laboratory frame after calculating the Lie brackets such that

$$\langle U_x^{(3)} \rangle = 0. \quad (6.25)$$

The zero velocity contributions at third order are similar to those of the classical Taylor sheet (Taylor 1951), but are different from the uniform compression case.

The case $\phi = \pi/2$ can also be calculated in a similar manner. By executing the second-order calculations, we found that the expression of the averaged progressive velocity $\langle U_x \rangle$

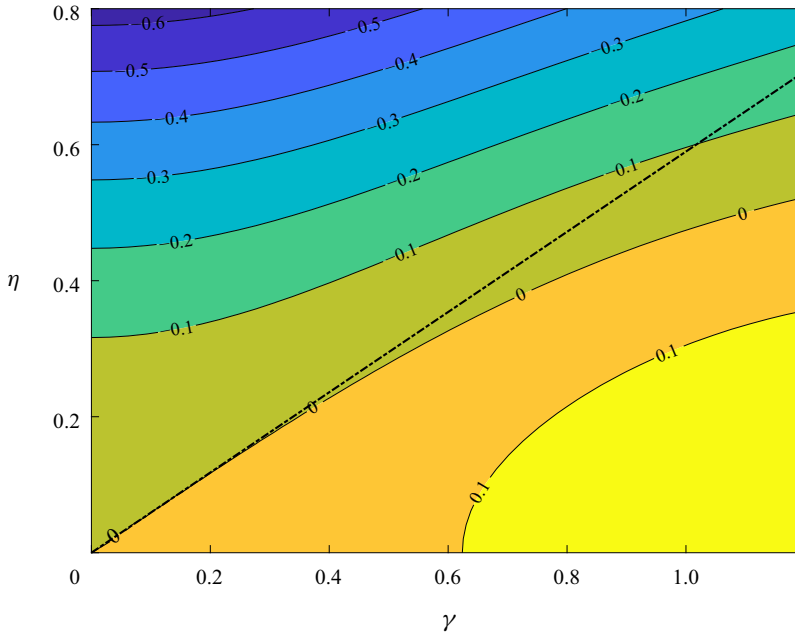


Figure 9. Numerical simulation of averaged swimming velocity $\langle U_x \rangle$ (in the reference frame) of the swimmer driven by a symmetrical compression wave with $L_0 = 1$, $kL = 2\pi$, $\phi = \pi/2$ and $\omega = 2\pi$ for different values of ϵ and η . The dashed line is a null curve of the velocity predicted by the small-amplitude theory up to third order, which is in excellent agreement when $\epsilon \lesssim 0.4$.

is identical to that obtained in the $\phi = 0$ case (6.23), together with zero normal and rotational velocities due to the symmetry. At third order, the progressive velocity has a form similar to (6.24), i.e.

$$\langle \tilde{U}_x^{(3)} \rangle = -\frac{3\epsilon^2\eta\omega}{2k^2L_0^2}, \quad (6.26)$$

and after including the non-commutative effects from the Lie bracket, this contribution vanishes again: $\langle U_x^{(3)} \rangle = 0$.

Hence both when $\phi = 0$ and $\phi = \pi/2$, according to the analysis above (see (6.23)), net locomotion disappears when

$$\left| \frac{\eta}{\epsilon} \right| = \sqrt{\left(1 - \frac{12}{k^2L_0^2} \right) \frac{\gamma - 1}{2}}. \quad (6.27)$$

To test these theoretical results, we numerically compute the averaged swimming velocity for a finite amplitude with different ϵ and η , with the same numerical scheme as in § 5. The results are shown in figure 9, together with the theoretical prediction of the null curve by the small-amplitude theory (6.27). As seen in the figure, the theoretical prediction is in excellent agreement when $\epsilon \lesssim 0.4$.

7. Manoeuvrability by bending–compression in different drag environments

In the previous sections, we have seen that a phase difference between the bending and compression modes may generate swimmer rotation. To further qualitatively examine

the manoeuvrability of extensible swimmers, in this section, we evaluate the power consumption for drift and turning motion in the small-amplitude model, and compare the turning dynamics by bending–compression coupling with those of inextensible slender swimmers. Moreover, we numerically highlight the important role of the anisotropy drag ratio γ to plan the swimmer’s motion after a gait.

Inextensible microswimmers with cilia and flagella control their orientation by laterally asymmetric beating, as seen in chemotactic sperm cells (Shiba *et al.* 2008). To represent an asymmetric waveform, we consider a non-zero mean curvature in the bending angle as

$$\tilde{\theta}(s_0, t) = \epsilon q(s_0, t) + \kappa s_0, \quad (7.1)$$

where a constant κ corresponds to the mean curvature in the absence of compression.

We first perform perturbation analysis with the small-amplitude theory in §4, by assuming $\epsilon, \eta, \kappa \ll 1$, $\eta = O(\epsilon)$ and $\kappa = O(\epsilon)$. Following the previous analyses in §§5 and 6, we consider functions of $p(s_0, t)$ and $q(s_0, t)$ for uniform compression (5.1) and bending–compression wave (6.1). With the assumptions of the integer number of waves, $kL_0 = \pm 2\pi, \pm 4\pi, \dots$, the difference in the tangent angle is simply $\tilde{\theta}(L_0, t) - \tilde{\theta}(0, t) = \kappa L_0$.

We then redo the perturbation calculations of §§5 and 6, including the non-zero mean curvature. The resulting expressions reveal that in both the uniform compression and bending–compression wave cases, the time-averaged translational and rotational velocities are unchanged up to the second order of expansion, regardless of the non-zero mean curvature. In particular, the lateral and rotational velocities are $\langle U_y \rangle = O(\epsilon\eta)$ and $\langle \Omega \rangle = O(\epsilon\eta)$, respectively, and the effects of κ only appear in the higher-order averaged velocities. Moreover, we note that $O(\epsilon\kappa)$ terms appear in the instantaneous velocities, but all vanish by taking the time average. This quantitatively demonstrates the importance of the compression-driven turning in terms of swimmer manoeuvrability compared to asymmetric inextensible bending.

Further, the energy consumption $\langle P \rangle = \langle \int \mathbf{f}(s) \cdot \mathbf{u}(s) ds \rangle$ may be computed analytically from the small-amplitude theory. We find, in both the uniform compression wave and bending–compression wave, the identical leading-order expression

$$\langle P \rangle \propto \frac{\omega^2 L_0}{2k^2} \left(1 - \frac{12}{k^2 L_0^2} \right) \gamma \epsilon^2 + \frac{\omega^2 L_0}{2k^2} \eta^2, \quad (7.2)$$

in the non-symmetrised case, where the frequencies of bending and compression are equal. Here, the overall constant prefactor is omitted. In line with Lighthill (1976), a possible definition of swimming efficiencies (a rate of energetic conversion) may be

$$\text{Eff}_{\text{prog}} = C_{\parallel} L_0 \langle U_x \rangle / \langle P \rangle, \quad (7.3)$$

$$\text{Eff}_{\text{drift}} = C_{\perp} L_0 \langle U_y \rangle / \langle P \rangle, \quad (7.4)$$

$$\text{Eff}_{\text{turn}} = C_R L_0^2 \langle \Omega \rangle / \langle P \rangle \quad (7.5)$$

for progressive, drifting and turning efficiencies, respectively, where C_R is the rotational drag coefficient. It is worth mentioning that the progressive efficiency is always smaller than the inextensible swimmer in the uniform compression case, because the compression does not contribute to the progressive speed (5.12). From the small-amplitude theory, the drifting and turning efficiencies have the form $a\epsilon\eta/(b\epsilon^2 + c\eta^2)$, where a , b and c are independent of the amplitudes ϵ and η . Therefore, we may find the optimal ratio of η and ϵ from the expression of $\langle P \rangle$ as

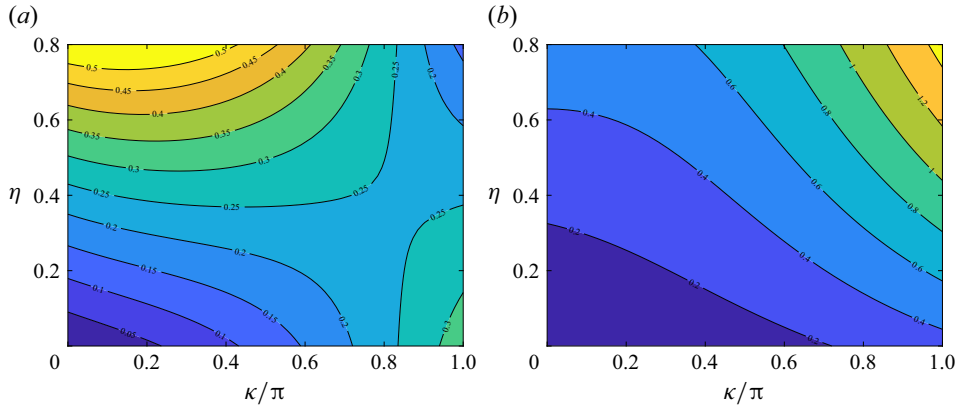


Figure 10. Numerical simulation of averaged angular velocity $\langle \Omega \rangle$ (in the reference frame) of the swimmer driven by (a) uniform compression wave and (b) bending-compression wave with $L_0 = 1$, $kL = 2\pi$ and $\omega = 2\pi$, $\epsilon = 0.4$, $\phi = 0.5\pi$ for different values of $\kappa \in [0, \pi]$ and $\eta \in [0, 0.8]$.

$$\frac{\eta}{\epsilon} = \left(1 - \frac{12}{k^2 L_0^2} \right)^{-1/2}. \quad (7.6)$$

We then examine the swimmer manoeuvrability for the finite-amplitude case by numerically evaluating the time-averaged rotational velocity for different values of η and κ , while the other parameters are fixed. In figure 10, we show an example of the contour plot of $\langle \Omega \rangle$ for the uniform compression (figure 10a) and bending-compression (figure 10b) cases. In both cases, the contour is rather horizontal in the small- κ regime, suggesting that asymmetric beating with non-zero mean curvature could be less efficient than bending-compression coupling to generate net rotation.

In addition to the deformation gait, the environment properties modelled by the anisotropic drag ratio γ also strongly impact the swimmer's manoeuvres. Recalling Proposition 1, uniform compression in isotropic drag cannot produce net locomotion. This is numerically confirmed as seen in figure 11(a), where we plot positions and orientations after one beat cycle of a uniform compression swimmer with different values of γ from 0.2 to 40 ($\gamma \in \{0.2, 0.4, \dots, 1.8, 2.0\} \cup \{3, 4, \dots, 40\}$). Initially, the position \mathbf{X} is taken at the origin, and the orientation angle Θ is set to zero, as shown by the black dot and the black arrow. After one beat cycle, the swimmer moves towards the $+x$ direction with positive lateral migration ($+y$ direction) when $\gamma < 1$, and the direction of the lateral motion is reversed when $\gamma > 1$, while no displacement and rotation are generated when $\gamma = 1$. In the bending-compression wave case, as shown in figure 11(b), the swimmer may move in both positive and negative x directions, and the net displacement and rotation are both generated even when $\gamma = 1$, as predicted by the small-amplitude theory.

8. Conclusions

We have theoretically investigated the impact of compression or extension on the bending motion of slender objects at low Reynolds number, with a particular focus on the bending-compression coupling effects, motivated by some biological and artificial microswimmers that exhibit a large amount of compression and extension.

We first revisited the effect of body extensibility on swimming with isotropic drag, first discussed by Pak & Lauga (2011), refining the arguments to prove that no net motion is possible by uniform compression with an isotropic drag (Proposition 1). Since the

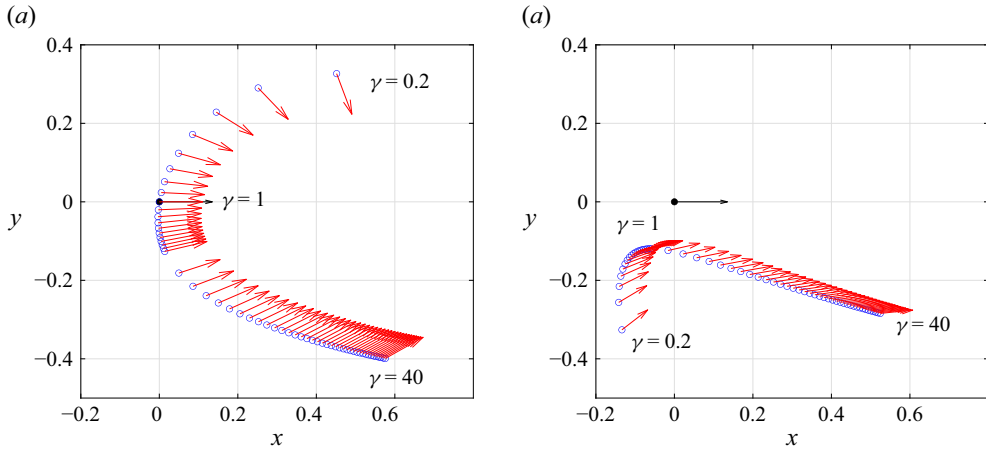


Figure 11. Positions and orientation, \mathbf{X} and Θ , after one beat period T for (a) uniform compression and (b) bending–compression wave with different γ values. The positions and orientations are depicted by blue circles and red arrows, respectively. Initial position $(0, 0)$ is marked by a black dot, and the initial orientation $\Theta = 0$ is shown by the black arrow. Parameters are the same as in figures 4(b) and 8(b): $\epsilon = \eta = 0.4$, $L_0 = 1$, $kL_0 = 2\pi$ and $\omega = 1$. The value of γ is changed from $\gamma = 0.2$ to $\gamma = 40$.

bending–compression coupling, in general, generates an instantaneous rotation or yawing motion, we employed the gauge theoretic formulation and the Lie bracket to deal with the rotation–translational coupling.

We then introduced minimal theoretical models with two degrees of freedom, one from bending and the other from compression/extension. The first model, which we referred to as the compressive scallop swimmer, undergoes uniform compression. The second minimal model, which we introduced as a ‘squeeze-me-bend-you’ swimmer, has a constant total length, but the position of the hinge can vary over time. We computed the curvature field that characterises the locomotion, and the results illustrated several deformation modes to generate translation and rotation, highlighting the enhancement of manoeuvrability and complexity of emergent dynamics through the compression during swimming.

We then examined a general slender body, with systematic perturbation analyses within the small-amplitude regime both for bending angle amplitude ϵ and compression amplitude η , with $\epsilon, \eta \ll 1$. As counterpart examples to the minimal models, we theoretically and numerically examined in detail the uniform compression as well as the bending–compression travelling wave, both being motivated by biological swimmers and relevant also in robotics.

The results are summarised in table 1. The analysis shows that bending–compression coupling triggers transverse drift and turning behaviours, at the order of $O(\epsilon\eta)$. With the coupling effects, the swimmer can make a turn, although the emergent behaviours depend on the phase shift between the bending and compression. This result highlights the importance of the shape gait symmetry, and we have found that net locomotion is only generated by the breakdown of symmetry.

To focus on the progressive velocity of the swimmer, we then considered uniform compression with a double frequency. Detailed perturbation analysis found that the bending–compression coupling appears as the increase or decrease of swimming speed at the order of $O(\epsilon^2\eta)$ in the uniform compression case, while the higher-order contributions vanish for the bending–compression wave case. In both cases, the theoretical prediction

Case Section	Uniform compression			Bending–compression wave		
	$\phi = 0, \pi$ § 5.1	$\phi \neq 0, \pi$ § 5.1	Symmetric § 5.2	$\phi = 0$ § 6.1	$\phi = \pi/2$ § 6.2	Symmetric § 6.3
$\langle U_x^{(2)} \rangle$	ϵ^2	ϵ^2	ϵ^2	$\epsilon^2 + \eta^2$	$\epsilon^2 + \eta^2$	$\epsilon^2 + \eta^2$
$\langle U_x^{(3)} \rangle$	–	–	$\epsilon^2 \eta$	–	–	0
$\langle U_y^{(2)} \rangle$	$\epsilon \eta$	$\epsilon \eta$	0	$\epsilon \eta$	$\epsilon \eta$	0
$\langle \Omega^{(2)} \rangle$	0	$\epsilon \eta$	0	0	$\epsilon \eta$	0

Table 1. Summary of the orders of magnitude appearing in the small-amplitude analysis. Amplitudes of bending and compression are denoted as η and ϵ , respectively.

well explained the numerical simulations, illustrating the usefulness of the systematic perturbation analysis incorporating the non-commutative effects of translation and rotation through the higher-order Lie brackets. Such a non-commutative effect has long been neglected in theoretical calculations of microswimmer models such as the Taylor sheet and slender filaments, for example by assuming an infinite body length and one-dimensional locomotion. In contrast, we have explicitly derived the finite-size effect of a slender bending filament at the Stokesian regime. The motion non-commutativity is inevitable for finite-sized bending swimmers that possess in general instantaneous lateral and rotational velocities. Such yawing effects in microswimmers are usually considered rapid time scale dynamics and often naively averaged out. However, if the swimmer dynamics is coupled with outer environments, then the long-time behaviour is no longer a simple average due to nonlinear interactions. This has been recently studied through multiple scale analysis for coupling with external flows, boundaries, neighbours and spatial viscosity variations (Walker *et al.* 2022*a,b*, 2023; Kanazawa & Ishimoto 2024).

Several extensions of the framework presented in this paper may be envisioned. As mentioned in § 2, we circumscribed our study to the kinematic problem, where deformation is prescribed. In the elastohydrodynamic problem, by contrast, deformation is an unknown, and a description of the internal active forcing and constitutive law of the deformable body, as well as suitable boundary conditions, is required to close the dynamics equations (e.g. Passov & Or 2012; Ramasamy & Hatton 2021; Ishimoto, Moreau & Yasuda 2023; Alouges *et al.* 2025; Ishimoto, Moreau & Herault 2025). Of course, it is challenging to observe, measure and model those internal forces in biological swimmers. Therefore, the dynamic problem, known as active elastohydrodynamics, is less straightforward. We hope to be able to solve the inverse problem of finding which internal activity can give rise to a prescribed bending–compression deformation in future studies. Another avenue of follow-up research would be to investigate the role of shear deformation in efficient locomotion. While less prominent as an active locomotion mechanism, transverse shear in slender bodies is studied in microscopic organisms (Gadêlha *et al.* 2013). It would be interesting to explore its role in locomotion using the same minimal model approach.

Our results on bending–compression coupling unveiled emergent drifting and rotation dynamics as well as modulations of progressive velocity by nonlinear interactions, which could be beneficial for higher manoeuvrability of locomotion. Also, these findings will be useful for better understanding of biological functionality in microswimmers with compression and extensibility (Yanase *et al.* 2018; Wan 2019; Cammann *et al.* 2025), as well as for designing soft artificial microrobots using the compression/extension degree of freedom, such as hydrogels (Nocentini *et al.* 2018). Our study sheds light on compression as an important degree of freedom in locomotion at low Reynolds number,

and more broadly in a dissipative medium, including slithering and crawling animals on the ground. Also, the theoretical methodology based on the geometrical formulation of microswimming will be widely applicable to yawing behaviours and non-commutative translation–rotation coupling in microswimming.

Funding. K.I. acknowledges the Japan Society for the Promotion of Science (JSPS) KAKENHI (grant nos 21H05309 and 24K21517) and the Japan Science and Technology Agency (JST), FOREST (grant no. JPMJFR212N). J.H. and C.M. acknowledge funding overseen by the French National Research Agency (ANR) and France 2030 as part of the Organic Robotics Programme (PEPR O2R).

Declaration of interests. The authors report no conflict of interest.

REFERENCES

- ALOUGES, F., ANELLO, I., DESIMONE, A., LEFEBVRE-LEPOT, A. & LEVILLAIN, J. 2025 Some mathematical models for flagellar activation mechanisms. *Math. Models Methods Appl. Sci.* **35**, 2395–2424.
- AMBROSE, W. & SINGER, I.M. 1953 A theorem on holonomy. *Trans. Am. Math. Soc.* **75** (3), 428–443.
- ARROYO, M., HELTAI, L., MILLÁN, D. & DESIMONE, A. 2012 Reverse engineering the euglenoid movement. *Proc. Natl Acad. Sci. USA* **109** (44), 17874–17879.
- ASADZADEH, S.S., WALTHER, J.H., ANDERSEN, A. & KJØRBOE, T. 2022 Hydrodynamic interactions are key in thrust-generation of hairy flagella. *Phys. Rev. Fluids* **7** (7), 073101.
- AVRON, J.E., KENNETH, O. & OAKNIN, D.H. 2005 Pushmepullyou: an efficient micro-swimmer. *New J. Phys.* **7** (1), 234.
- AVRON, J.E. & RAZ, O. 2008 A geometric theory of swimming: Purcell’s swimmer and its symmetrized cousin. *New J. Phys.* **10** (6), 063016.
- BACKHOLM, M., RYU, W.S. & DALNOKI-VERESS, K. 2013 Viscoelastic properties of the nematode *Caenorhabditis elegans*, a self-similar, shear-thinning worm. *Proc. Natl Acad. Sci. USA* **110** (12), 4528–4533.
- BASS, C., RAMASAMY, S. & HATTON, R.L. 2022 Characterizing error in noncommutative geometric gait analysis. In *2022 international conference on robotics and automation (ICRA)*, pp. 9845–9851. IEEE.
- BECKER, L.E., KOEHLER, S.A. & STONE, H.A. 2003 On self-propulsion of micro-machines at low Reynolds number: Purcell’s three-link swimmer. *J. Fluid Mech.* **490**, 15–35.
- BRENNEN, C. 1976 Locomotion of flagellates with mastigonemes. *J. Mechanochem. Cell Motil.* **3**, 207–217.
- CAMMANN, J., LAEVERENZ-SCHLOEGELHOFFER, H., WAN, K.Y. & MAZZA, M.G. 2025 Form and function in biological filaments: a physicist’s review. *Phil. Trans. R. Soc. A* **383**, 20240253.
- CHOLAKOVA, D., LISICKI, M., SMOUKOV, S.K., TCHOLAKOVA, S., LIN, E.E., CHEN, J., DE CANIO, G., LAUGA, E. & DENKOV, N. 2021 Rechargeable self-assembled droplet microswimmers driven by surface phase transitions. *Nat. Phys.* **17** (9), 1050–1055.
- CHONG, B., HE, J., LI, S., ERICKSON, E., DIAZ, K., WANG, T., SOTO, D. & GOLDMAN, D.I. 2023 Self-propulsion via slipping: frictional swimming in multilegged locomotors. *Proc. Natl Acad. Sci. USA* **120** (11), e2213698120.
- DESIMONE, A. & TATONE, A. 2012 Crawling motility through the analysis of model locomotors: two case studies. *Eur. Phys. J. E* **35**, 1–8.
- ELGETI, J., WINKLER, R.G. & GOMPPER, G. 2015 Physics of microswimmers – single particle motion and collective behavior: a review. *Rep. Prog. Phys.* **78** (5), 056601.
- FEBVRE-CHEVALIER, C. & FEBVRE, J. 1986 Motility mechanisms in the actinopods (protozoa): a review with particular attention to axopodial contraction/extension, and movement of nonactin filament systems. *Cell Motil. Cytoskel.* **6** (2), 198–208.
- FLAUM, E. & PRAKASH, M. 2024 Curved crease origami and topological singularities enable hyperextensibility of *L. olor*. *Science* **384** (6700), eadk5511.
- FRIEDRICH, B.M., RIEDEL-KRUSE, I.H., HOWARD, J. & JÜLICHER, F. 2010 High-precision tracking of sperm swimming fine structure provides strong test of resistive force theory. *J. Exp. Biol.* **213** (8), 1226–1234.
- FU, H.C., POWERS, T.R. & WOLGEMUTH, C.W. 2007 Theory of swimming filaments in viscoelastic media. *Phys. Rev. Lett.* **99** (25), 258101.
- GADÉLHA, H., GAFFNEY, E.A. & GORIELY, A. 2013 The counterbend phenomenon in flagellar axonemes and cross-linked filament bundles. *Proc. Natl Acad. Sci. USA* **110** (30), 12180–12185.
- GIDONI, P., MORANDOTTI, M. & ZOPPELLO, M. 2024 Gait controllability of length-changing slender microswimmers. *Maths Mech. Complex Syst.* **12** (4), 471–505.

- GRAY J. & HANCOCK G.J. 1955 The propulsion of sea-urchin spermatozoa. *J. Expl Biol.* **32** (4), 802–814.
- HATTON, R.L. & CHOSSET, H. 2015 Nonconservativity and noncommutativity in locomotion: geometric mechanics in minimum-perturbation coordinates. *Eur. Phys. J. Special Topics* **224** (17), 3141–3174.
- HUANG, B. & PITEKKA, D.R. 1973 The contractile process in the ciliate, *Stentor coeruleus*: I. The role of microtubules and filaments. *J. Cell Biol.* **57** (3), 704–728.
- ISHIMOTO, K. & GAFFNEY, E.A. 2018 An elastohydrodynamical simulation study of filament and spermatozoan swimming driven by internal couples. *IMA J. Appl. Maths* **83** (4), 655–679.
- ISHIMOTO K., MOREAU C., & HERAULT, J. 2025 Robust undulatory locomotion through neuromechanical adjustments in a dissipative medium. *J. R. Soc. Interface* **22** (222), 20240688.
- ISHIMOTO, K., MOREAU, C., & YASUDA, K. 2022 Self-organized swimming with odd elasticity. *Phys. Rev. E* **105** (6), 064603.
- ISHIMOTO, K., MOREAU, C., & YASUDA, K. 2023 Odd elastohydrodynamics: non-reciprocal living material in a viscous fluid. *PRX Life* **1** (2), 023002.
- ISHIMOTO, K. & YAMADA, M. 2012 A coordinate-based proof of the scallop theorem. *SIAM J. Appl. Maths* **72** (5), 1686–1694.
- IZQUIERDO, E.J. & BEER, R.D. 2018 From head to tail: a neuromechanical model of forward locomotion in *Caenorhabditis elegans*. *Phil. Trans. R. Soc. B: Biol. Sci.* **373** (1758), 20170374.
- KANAZAWA, T. & ISHIMOTO, K. 2024 Locomotion on a lubricating fluid with spatial viscosity variations. *Phys. Rev. Fluids* (arXiv preprint [arXiv:2412.15656](https://arxiv.org/abs/2412.15656)).
- KEAVENY, E.E. & BROWN, A.E.X. 2017 Predicting path from undulations for *C. elegans* using linear and nonlinear resistive force theory. *Phys. Biol.* **14** (2), 025001.
- KELLY, S.D. & MURRAY, R.M. 1995 Geometric phases and robotic locomotion. *J. Robotic Syst.* **12** (6), 417–431.
- KOENS, L. & LAUGA, E. 2016 Rotation of slender swimmers in isotropic-drag media. *Phys. Rev. E* **93** (4), 043125.
- LAUGA, E. 2020 *The Fluid Dynamics of Cell Motility*, Cambridge University Press.
- LIGHTHILL, J. 1976 Flagellar hydrodynamics. *SIAM Rev.* **18** (2), 161–230.
- LISICKI, M. 2024 Twist and turn: elastohydrodynamics of microscale active fibres. *Eur. Phys. J. Special Topics* **223**, 2775–2808.
- MENEELY, P.M., DAHLBERG, C.L. & ROSE, J.K. 2019 Working with worms: *Caenorhabditis elegans* as a model organism. *Curr. Protocols Essential Lab. Techniques* **19** (1), e35.
- MONTENEGRO-JOHNSON, T.D., GAGNON, D.A., ARRATIA, P.E. & LAUGA, E. 2016 Flow analysis of the low Reynolds number swimmer *C. elegans*. *Phys. Rev. Fluids* **1** (5), 053202.
- MOREAU, C. 2019 Local controllability of a magnetized Purcell’s swimmer. *IEEE Control Syst. Lett.* **3** (3), 637–642.
- MOREAU, C., GIRALDI, L. & GADÉLHA, H. 2018 The asymptotic coarse-graining formulation of slender-rods, bio-filaments and flagella. *J. R. Soc. Interface* **15** (144), 20180235.
- NAJAFI, A. & GOLESTANIAN, R. 2004 Simple swimmer at low Reynolds number: three linked spheres. *Phys. Rev. E* **69** (6), 062901.
- NIKOLOV, S.V., YEH, P.D. & ALEXEEV, A. 2015 Self-propelled microswimmer actuated by stimuli-sensitive bilayered hydrogel. *ACS Macro Lett.* **4** (1), 84–88.
- NOCENTINI, S., PARMEGGIANI, C., MARTELLA, D. & WIERMSMA, D.S. 2018 Optically driven soft micro robotics. *Adv. Opt. Mater.* **6** (14), 1800207.
- NOMURA, M., ATSUJI, K., HIROSE, K., SHIBA, K., YANASE, R., NAKAYAMA, T., ISHIDA, K.-I. & INABA, K. 2019 Microtubule stabilizer reveals requirement of Ca^{2+} -dependent conformational changes of microtubules for rapid coiling of haptoneuma in haptophyte algae. *Biol. Open* **8** (2), bio036590.
- OLSON, S.D., LIM, S. & CORTEZ, R. 2013 Modeling the dynamics of an elastic rod with intrinsic curvature and twist using a regularized Stokes formulation. *J. Comput. Phys.* **238**, 169–187.
- PAK, O.S. & LAUGA, E., 2011 Extensibility enables locomotion under isotropic drag. *Phys. Fluids* **23** (8), 081702.
- PAK, O.S., SPAGNOLIE, S.E. & LAUGA, E. 2012 Hydrodynamics of the double-wave structure of insect spermatozoa flagella. *J. R. Soc. Interface* **9** (73), 1908–1924.
- PASSOV, E. & OR, Y. 2012 Dynamics of Purcell’s three-link microswimmer with a passive elastic tail. *Eur. Phys. J. E* **35** (8), 78.
- PURCELL, E.M. 1977 Life at low Reynolds number. *Am. J. Phys.* **45**, 3–11.
- RAMASAMY S. & HATTON R.L. 2021 Optimal gaits for drag-dominated swimmers with passive elastic joints. *Phys. Rev. E* **103** (3), 032605.
- RIESER, J.M. 2024 Geometric phase predicts locomotion performance in undulating living systems across scales. *Proc. Natl Acad. Sci. USA* **121** (24), e2320517121.

- RILEY, E.E. & LAUGA, E. 2017 Empirical resistive-force theory for slender biological filaments in shear-thinning fluids. *Phys. Rev. E* **95** (6), 062416.
- ROUSSEL, N., SPRENGER, J., TAPPAN, S.J. & GLASER, J.R. 2014 Robust tracking and quantification of *C. elegans* body shape and locomotion through coiling, entanglement, and omega bends. *Worm* **3**, e982437.
- RYU, S., PEPPER, R., NAGAI, M., & FRANCE, D. 2016 Vorticella: a protozoan for bio-inspired engineering. *Micromachines-BASEL* **8** (1), 4.
- SHAMMAS, E.A., CHOSSET, H. & RIZZI, A.A. 2007 Geometric motion planning analysis for two classes of underactuated mechanical systems. *Intl J. Robot. Res.* **26** (10), 1043–1073.
- SHAPER, A. & WILCZEK, F. 1989 Geometry of self-propulsion at low Reynolds number. *J. Fluid Mech.* **198**, 557–585.
- SHARAN, P., MASLEN, C., ALTUNKEYIK, B., REHOR, I., SIMMCHEN, J. & MONTENEGRO-JOHNSON, T.D. 2021 Fundamental modes of swimming correspond to fundamental modes of shape: engineering I-, U-, and S-shaped swimmers. *Adv. Intell. Syst.* **3** (11), 2100068.
- SHIBA, K., BABA, S.A., INOUE, T. & YOSHIDA, M. 2008 Ca^{2+} bursts occur around a local minimal concentration of attractant and trigger sperm chemotactic response. *Proc. Natl Acad. Sci. USA* **105** (49), 19312–19317.
- SILVERBERG, O., DEMIR, E., MISHLER, G., HOSOUME, B., TRIVEDI, N., TISCH, C., PLASCENCIA, D., PAK, O.S. & ARACI, I.E. 2020 Realization of a push-me-pull-you swimmer at low Reynolds numbers. *Bioinspir. Biomim.* **15** (6), 064001.
- SUZAKI, T., SHIGENAKA, Y., WATANABE, S. & TOYOHARA, A. 1980 Food capture and ingestion in the large heliozoan, *Echinospheerium nucleofilum*. *J. Cell Sci.* **42** (1), 61–79.
- TAN, L., YANG, Y., FANG, L. & CAPPELLERI, D.J. 2024 Shape-programmable adaptive multi-material microswimmers for biomedical applications. *Adv. Funct. Mater.* **34** (34), 2401876.
- TANAKA, Y., ITO, K., NAKAGAKI, T. & KOBAYASHI, R. 2012 Mechanics of peristaltic locomotion and role of anchoring. *J. R. Soc. Interface* **9** (67), 222–233.
- TAYLOR, G.I. 1951 Analysis of the swimming of microscopic organisms. *Proc. R. Soc. Lond. A: Math. Phys. Sci.* **209** (1099), 447–461.
- WALKER, B.J., ISHIMOTO, K. & GAFFNEY, E.A. 2023 Systematic parameterizations of minimal models of microswimming. *Phys. Rev. Fluids* **8** (3), 034102.
- WALKER, B.J., ISHIMOTO, K., GAFFNEY, E.A., MOREAU, C. & DALWADI, M.P. 2022a Effects of rapid yawing on simple swimmer models and planar Jeffery’s orbits. *Phys. Rev. Fluids* **7** (2), 023101.
- WALKER, B.J., ISHIMOTO, K., MOREAU, C., GAFFNEY, E.A. & DALWADI, M.P. 2022b Emergent rheotaxis of shape-changing swimmers in Poiseuille flow. *J. Fluid Mech.* **944**, R2.
- WAN, K.Y. 2019 Ciliate biology: the graceful hunt of a shape-shifting predator. *Curr. Biol.* **29** (22), R1174–R1176.
- YANASE, R., NISHIGAMI, Y., ICHIKAWA, M., YOSHIHISA, T. & SONOBE, S. 2018 The neck deformation of *Lacrymaria olor* depending upon cell states. *J. Protistol.* **51**, 1–6.
- YASUDA, K., HOSAKA, Y. & KOMURA, S. 2023 Generalized three-sphere microswimmers. *J. Phys. Soc. Japan* **92** (12), 121008.
- ZHANG, T. & GOLDMAN, D.I. 2014 The effectiveness of resistive force theory in granular locomotion. *Phys. Fluids* **26** (10), 101308.
- ZHAO, D., BITTNER, B., CLIFTON, G., GRAVISH, N. & REVZEN, S. 2022 Walking is like slithering: a unifying, data-driven view of locomotion. *Proc. Natl Acad. Sci. USA* **119** (37), e2113222119.